

Objective Evaluation of Satellite Precipitation Datasets for Heavy Precipitation Events Caused by Typhoons in the Philippines

Putu Aryastana

National Central University

Chian-Yi Liu (✉ cylui7@gate.sinica.edu.tw)

Academia Sinica <https://orcid.org/0000-0003-1725-4405>

Ben Jong-Dao Jou

National Taiwan University

Esperanza Cayanan

Philippine Atmospheric, Geophysical and Astronomical Services Administration

Jason Pajimola Punay

National Central University

Research article

Keywords: GSMaP, heavy precipitation, IMERG, PERSIANN, Philippines, typhoon

Posted Date: July 14th, 2021

DOI: <https://doi.org/10.21203/rs.3.rs-684518/v1>

License: © ⓘ This work is licensed under a Creative Commons Attribution 4.0 International License.

[Read Full License](#)

47 **Key Points/Highlights:**

- 48 1. Satellite precipitation datasets during five typhoon-related heavy precipitation
49 events in the Philippines were evaluated for the first time.
- 50 2. The 34-knot wind radii of the typhoons were used to select rain gauge
51 measurements.
- 52 3. The satellite precipitation datasets were analyzed in terms of various rainfall
53 intensities, the terrain, and wind velocity effects.

54

55

56 **Running title:** Satellite precipitation datasets for heavy precipitation events caused by
57 typhoons in the Philippines

58

59

60 **Abstract**

61 Extreme weather events, such as typhoons, have occurred more frequently in the
62 last few decades in the Philippines. The heavy precipitation caused by typhoons is
63 difficult to measure with traditional instruments, such as rain gauges and ground-based
64 radar, because these instruments have an uneven distribution in remote areas. Satellite
65 precipitation datasets (SPDs) provide integrated spatial coverage of rainfall
66 measurements, even for remote areas. This study performed subdaily (3-hour)
67 assessments of SPDs (i.e., the Integrated Multi-satellitE Retrievals for Global
68 Precipitation Measurement [IMERG], Global Satellite Mapping of Precipitation
69 [GSMaP], and Precipitation Estimation from Remotely Sensed Information Using
70 Artificial Neural Networks datasets) during five typhoon-related heavy precipitation
71 events in the Philippines between 2016 and 2018. The aforementioned assessments
72 were performed through a point-to-grid comparison by using continuous and
73 volumetric statistical validation indices for the 34-knot wind radii of the typhoons,
74 rainfall intensity, the terrain, and wind velocity effects. The results revealed that the
75 IMERG exhibited good agreement with rain gauge measurements and exhibited high
76 performance in detecting rainfall during five typhoon events, whereas the GSMaP
77 exhibited high agreement during peak rainfall. All the SPDs tended to overestimate
78 rainfall during light to moderate rainfall events and underestimate rainfall during heavy

79 to extreme events. The IMERG exhibited a strong ability to detect moderate rainfall
80 events (5–15 mm/3 hours), whereas the GSMaP exhibited superior performance in
81 detecting heavy to extreme rainfall events (15–25, 25–50, and >50 mm/3 hours). The
82 GSMaP exhibited the best performance for detecting heavy rainfall at high elevations,
83 whereas the IMERG exhibited the best performance for rainfall detection at low
84 elevations. The IMERG exhibited a strong ability to detect heavy rainfall under various
85 wind speeds. A strong ability to detect heavy rainfall events for different wind speeds
86 in the western and eastern parts of the mountainous region of Luzon were found for the
87 GSMaP and IMERG, respectively. This study demonstrated that the IMERG and
88 GSMaP datasets exhibit promising performance in detecting heavy precipitation caused
89 by typhoon events.

90

91

92 **Keywords:**

93 GSMaP, heavy precipitation, IMERG, PERSIANN, Philippines, typhoon

94

95

96

97 **1 Introduction**

98 Heavy precipitation refers to a rainfall event that occurs in a certain area; exceeds
99 a certain threshold; tends to be of short duration; can threaten human activity; and often
100 causes natural disasters (such as floods and landslides) that result in social problems,
101 environmental damage, and material losses (Bell et al. 2004; Hong et al. 2006; Wu et
102 al. 2012; Stampoulis et al. 2013; Chen and Wu 2016). Heavy precipitation can be
103 triggered by events such as tropical cyclones (typhoons) (Wang et al. 2016). Typhoons
104 can cause heavy precipitation from the eye to the eyewall of the storm, a distance that
105 can be tends to hundreds of kilometers across (Lonfat et al. 2007; Kimball 2008;
106 Yokoyama and Takayabu 2008; Wang et al. 2009). Typhoons can also cause heavy
107 rainfall in distant regions located thousands of kilometers from the center of a typhoon
108 (Ross and Kurihara 1995; Wang et al. 2009; Chen and Wu 2016). The quantity of
109 rainfall caused by typhoons is affected by several factors, such as the internal typhoon
110 structure, track variations, large-scale moisture convergence, convection strength,
111 cloud microphysics, typhoon interaction at midlatitude, and typhoon interaction with
112 the topography (Jones et al. 2003; Wu et al. 2009; Zhang et al. 2010; Yang et al. 2011;
113 Yu and Cheng 2013; Huang and Lin 2014; Chen and Wu 2016; Cheung et al. 2018;
114 Hon, 2020). Because the diameters of typhoons range from 100 to 2000 km, monitoring
115 the heavy rainfall caused by typhoons with conventional instruments is difficult (Huang

116 et al. 2019). Therefore, achieving an accurate quantitative estimation of heavy rainfall
117 caused by typhoon events represents the largest challenge in hydrometeorological
118 research and natural disaster modeling.

119 The analysis of heavy precipitation requires an accurate precipitation dataset with
120 global coverage as well as high spatial and temporal resolutions (Setiawati et al. 2016;
121 Liu et al. 2019; Liu et al. 2020a). Accurate rainfall data with high spatial and temporal
122 resolution at regional and global scales are difficult to access in the fields of hydrology
123 and weather forecasting. In situ measurements from rain gauge stations can supply
124 reliable point-scale rainfall data (Duan et al. 2016). However, rain gauge stations are
125 unevenly distributed, with few such stations being found in remote and mountainous
126 areas, which limits the quantity of accurate spatial and temporal data that can be
127 obtained for these areas (Javanmard et al. 2010; Ji et al. 2020). Weather radar can
128 provide local precipitation data with sufficiently high spatial and temporal resolution.
129 However, these data are affected by deviations from electromagnetic signals due to the
130 effect of the terrain in mountainous areas (Li et al. 2013).

131 The rapid development of remote sensing techniques in the fields of hydrology
132 and meteorology has resulted in the development of several satellite-based precipitation
133 estimation methods with global coverage as well as high spatial and temporal resolution
134 (Wu et al. 2019; Nashwan et al. 2020). Satellite precipitation datasets (SPDs) released

135 online to the public can overcome the problem caused by the unavailability of rain
136 gauge station and weather radar data. Rainfall estimation techniques using SPDs are
137 broadly based on the thermal infrared (TIR) radiation of geostationary satellites, the
138 passive microwave (PMW) radiations recorded by sensors in low Earth orbiting
139 satellites, or a combination of TIR and PMW radiations (Duan et al. 2016; Liu et al.
140 2019; Levizzani and Cattani 2019). These estimation techniques are not perfect in terms
141 of accurately predicting rainfall intensity. Therefore, calibration and validation are
142 necessary before SPDs can be used for hydrological modeling or meteorological
143 disaster observation. Global coverage can be achieved by several SPDs, such as the
144 Precipitation Estimation from Remotely Sensed Information Using Artificial Neural
145 Networks (PERSIANN; Hsu et al. 1997), the Climate Prediction Center Merged
146 Analysis of Precipitation (Xie and Arkin 1997), the Climate Prediction Center
147 Morphing Algorithm (CMORPH; Joyce et al. 2004), the Global Satellite Mapping of
148 Precipitation (GSMaP; Okamoto et al. 2005), the Integrated Multi-satellitE Retrievals
149 for Global Precipitation Measurement (IMERG; Hou et al. 2014), the Climate Hazards
150 Group InfraRed Precipitation with Station (CHIRPS; Funk et al. 2015), and the
151 Multisource Weighted-Ensemble Precipitation (Beck et al. 2017) datasets.

152 Revisions in the algorithms of SPDs had been made based on key studies which
153 improved the capability of SPDs in detecting heavy rainfall. Studies have evaluated the

154 performance of the Tropical Rainfall Measuring Mission (TRMM) 3B42 dataset during
155 an extreme rainfall event (Pombo and de Oliveira 2015; Parida et al. 2017; Huang et al.
156 2018; Rashid et al. 2018; Liu et al. 2019; Palharini et al. 2020). Pombo and de Oliveira
157 (2015) evaluated the performance of the TRMM 3B42 dataset in estimating the annual
158 maximum daily rainfall in Angola. They discovered that the TRMM 3B42 dataset
159 showed promise for the estimation of heavy precipitation events. The TRMM 3B42
160 dataset provided underestimated values compared with the rain gauge measurements.
161 In a previous study, compared with rain gauge measurements for heavy precipitation
162 events during June 2013 in the Western Himalayas, the TRMM 3B42 and CMORPH
163 datasets underestimated the daily rainfall and peak rainfall intensity, whereas the
164 GSMaP dataset both overestimated and underestimated rainfall values (Parida et al.
165 2017). The TRMM 3B42 dataset exhibited a promising ability to determine the monthly
166 maximum 1-day precipitation, monthly maximum 2-day consecutive precipitation,
167 monthly maximum 5-day consecutive precipitation, and total annual precipitation for
168 wet days in China between 2009 and 2013 (Huang et al. 2018). For flooding caused by
169 heavy rainfall from September 1 to September 7, 2014, in the Kashmir Valley in India,
170 the TRMM 3B42 and GSMaP datasets underestimated rainfall, whereas the IMERG
171 dataset demonstrated superior performance to that of the rain gauges in terms of daily
172 estimation, with high correlation and Nash–Sutcliffe coefficients and the lowest bias

173 value (Rashid et al. 2018). TRMM 3B42 version 7 outperformed the PERSIANN and
174 CMORPH datasets in terms of accuracy of detecting monthly and annual heavy
175 precipitation events from 2009 to 2014 in the Wei River Basin in China (Liu et al. 2019).
176 The calibrated rain gauge of the TRMM, GSMaP, CMORPH, CHIRPS, and
177 PERSIANN datasets outperformed compare to the near-real-time of each datasets in
178 terms of estimating heavy rainfall in South America from 2012 to 2016 (Palharini et al.
179 2020). The accuracy of the CMORPH dataset was higher than that of the PERSIANN
180 dataset in terms of radar precipitation observations of heavy rainfall during seven major
181 flood events in regions of various terrains in northern Italy and southern France between
182 2003 and 2008 (Stampoulis et al. 2013). The GSMaP near-real-time dataset calibrated
183 by gauges outperformed the uncalibrated dataset in terms of estimating daily and
184 weekly heavy precipitation in East Asia and the Western Pacific from April 2000 to
185 March 2019 (Tashima et al. 2020). Studies have investigated the ability of SPDs to
186 measure heavy precipitation events on daily, monthly, seasonal, and annual scales.
187 Therefore, the ability of SPDs to measure heavy participation on a subdaily (3-hour)
188 scale must be investigated.

189 Several studies have compared the abilities of SPDs and rain gauges to measure
190 typhoon-related heavy precipitation events. Yu et al. (2009) performed 6-hourly and
191 daily evaluations of TRMM 3B42 version 6, the CMORPH dataset, and the

192 Geostationary Meteorological Satellite-5 infrared brightness temperature dataset in
193 mainland China by using descriptive and categorical statistics. Chen et al. (2013)
194 validated the TRMM, PERSIANN, and CMORPH datasets at various spatial and
195 temporal resolutions for the extreme 2009 Typhoon Morakot in Taiwan by using
196 descriptive and categorical statistics. Wang et al. (2016) evaluated the integrated
197 rainfall data derived from the Climate Prediction Center morphing technique and gauge
198 observations in terms of the estimation of heavy precipitation related to seven typhoon
199 events by using rain gauge stations in areas within 400 km of the typhoon center. Huang
200 et al. (2019) investigated the accuracy of the IMERG Early and Final Run datasets in
201 terms of the probability distribution of precipitation rates, spatiotemporal variability,
202 bias analysis, and contingency scores to detect heavy rainfall caused by six typhoons in
203 the coastal area of the Pearl River Delta in southern China. Pham and Vu (2020)
204 examined the horizontal and vertical precipitation structures of typhoons in the central
205 coastal areas of Vietnam by using the TRMM and GSMaP datasets. Various studies
206 that have compared the abilities of SPDs to detect heavy rainfall caused by landfalling
207 typhoons have suggested performing a comparison in terms of rainfall distribution and
208 spatiotemporal scale, analyzing rain gauges in areas within 400 km of the center of a
209 typhoon in coastal regions, and using descriptive and categorical statistics to perform

210 an analysis. Therefore, the effects of terrain and wind velocity on the ability of SPDs to
211 detect heavy precipitation caused by typhoons must be investigated.

212 The Philippines is an archipelago with more than 7100 islands of complex
213 topography (Ramos et al. 2016; Bagtasa 2017). Two of its islands, namely Luzon in the
214 north and Mindanao in the south, have long chains of mountains, whereas the Visayas
215 region, which is located in the center of the country, consists of small islands (Ramos
216 et al. 2016; Bagtasa 2017). The Philippines frequently experiences typhoons that form
217 in the Northwestern Pacific Basin (Weinkle et al. 2012; Bagtasa, 2017). Every year,
218 approximately 19 typhoons cross the border of the Philippines, and half of these
219 typhoons make landfall (Cinco et al. 2016; Bagtasa 2017). Few studies have evaluated
220 the performance of SPDs for predicting precipitation in the Philippines. Jamandre and
221 Narisma (2013) investigated the error characteristics of the TRMM and CMORPH
222 datasets against the data of ground stations and the Asian Precipitation Highly-Resolved
223 Observational Data Integration Towards the Evaluation of Water Resources
224 (APHRODITE) gridded precipitation dataset from 2003 to 2005. Ramos et al. (2016)
225 evaluated the performance of the TRMM, CMORPH, GSMaP, and PERSIANN
226 datasets and compared their performance with that of measurements from 52 rain gauge
227 stations between 1998 and 2015. However, to the best of our knowledge, no study has
228 assessed the performance of SPDs during heavy precipitation events caused by

229 typhoons in the Philippines. Therefore, this study evaluated the performance of three
230 SPDs, namely the IMERG, GSMaP, and PERSIANN datasets, during five typhoon-
231 related heavy precipitation events in the Philippines between 2016 and 2018. The
232 current study evaluated the performance of the aforementioned SPDs by comparing
233 their data with those of ground rain gauges in terms of the 34-knot wind radius (R34)
234 of a typhoon, rainfall intensity, and the effects of terrain and wind velocity. Section 2
235 describes the study area. Section 3 provides a detailed description of the dataset and
236 methodology used in this study. Section 4 describes the performance of the three SPDs
237 in terms of rainfall intensity, terrain, and wind velocity effects. Finally, Section 5
238 summarizes our findings.

239

240 **2 Study Area**

241 The study area was the Philippines, which is located between 4°40'N and 21°10'N
242 and between 116°40'E and 126°34'E. This country has a total area of 300,055 km²
243 (Figure 1a). The Philippines is located off the southeast coast of continental Asia across
244 the South China Sea in the strategic zone between China, Taiwan, Borneo, and
245 Indonesia. The Philippines is surrounded by the sea and is the only Southeast Asian
246 country to not border neighboring countries (Bautista 2011). This country has a tropical
247 maritime climate, and its seasonal changes are influenced by northeast and southwest

248 monsoon activity (Cinco et al. 2016). The Philippines experiences a cool dry season
249 from December to February, a hot dry season from March to May, and a rainy season
250 from June to November (The Philippine Atmospheric, Geophysical and Astronomical
251 Services Administration [PAGASA]). Precipitation is the essential climatic factor of
252 the Philippines. The distribution of precipitation in the country differs from one region
253 to another and depends on the direction of moisture-bearing winds and the location of
254 mountain systems (PAGASA). The mean annual precipitation of the Philippines ranges
255 between 965 and 4064 mm per year (PAGASA). Precipitation in many areas of the
256 Philippines is also influenced by typhoons (Ramos et al. 2016). Particular areas in the
257 northern Philippines can receive approximately 50% to 60% of their annual
258 precipitation from passing typhoons (Kubota and Wang 2009).

259

260 **3 Datasets and Methods**

261 **3.1 Datasets**

262 The multisource datasets used in this study can be categorized into four types:
263 typhoon event data; traditional observational rainfall data obtained from surface rain
264 gauges; precipitation information estimated from satellite measurements; and wind
265 vector data, which constitute a reanalysis dataset. The following subsections provide a
266 brief description of these four types of data.

267 **3.1.1 Typhoon Events**

268 Table 1 presents brief descriptions of five typhoon events that passed over the
269 Philippines. The information regarding the typhoons was provided by the International
270 Best Track Archive for Climate Stewardship (IBTrACS). IBTrACS maintains an
271 archive of the typhoon best track data for specific locations to add to the knowledge on
272 the distribution, frequency, and intensity of typhoons worldwide. The World
273 Meteorological Organization Tropical Cyclone Programme has endorsed IBTrACS as
274 an official recording and distribution resource for typhoon best track data (Knapp et al.
275 2010). The typhoon best track data contain 3-hour and long-term typhoon positioning
276 records (from 1980 to the present). The typhoon track data are available online at
277 <https://climatedataguide.ucar.edu/climate-data/ibtracs-tropical-cyclone-best-track-data>.
278 The five typhoons analyzed in this study passed over Luzon island. Typhoons
279 Mangkhut and Haima passed through the north, Typhoon Sarika passed through the
280 middle, and typhoons Nock-ten and Doksuri passed through the south of the Luzon
281 island. The five typhoons were classified into various categories according to
282 PAGASA's tropical cyclone intensity scale, namely typhoons (Mangkhut, Sarika,
283 Haima, and Nock-ten), and tropical storms (Doksuri).

284 **3.1.2 Data from Rain Gauge Measurements**

285 The data from rain gauge measurements were used as a reference to evaluate the
286 performance of the SPDs. Three-hour rainfall observation data for typhoons making
287 landfall in the Philippines were obtained from PAGASA, the Department of Science
288 and Technology, the Republic of the Philippines. PAGASA provides rainfall data from
289 222 automatic weather stations distributed across the Philippines. A total of 66 rain
290 gauge stations were selected on the basis of whether the spatial distribution was affected
291 by the R34 values of the typhoons and the completeness of the desired data. Table 1
292 lists the number of selected rain gauge stations within the R34 during the passing of the
293 storm. PAGASA has made available high-quality rain gauge data for the five
294 considered typhoon events.

295 **3.1.3 IMERG Dataset**

296 The high-resolution IMERG dataset is an improvement on the TRMM
297 Multisatellite Precipitation Analysis dataset, whose global coverage data were made
298 available from June 2000. The IMERG program was initiated by the National
299 Aeronautics and Space Administration (NASA) and the Japan Aerospace Exploration
300 Agency (JAXA). Its algorithm intercalibrates, merges, and interpolates all available
301 satellite microwave precipitation measurements, microwave-calibrated infrared
302 measurements, surface rain gauge analyses, and other possible rainfall estimates on

303 wide temporal and spatial scales for nearly the entire globe (Huffman et al. 2019). The
304 IMERG dataset provides half-hourly, daily, and monthly rainfall estimation at a spatial
305 resolution of 0.1°. The IMERG dataset contains three types of data in terms of time
306 release, namely early-, late-, and final-run data. The time-release delay is 4 hours for
307 the early-run data, 12 hours for the late-run data, and 3.5 months for the final-run data
308 (Huffman et al. 2019). This study used the latest Level-3 IMERG half-hourly data from
309 version 06B of the final-run dataset. The final-run dataset exhibits superior performance
310 to that of the early- and late-run datasets. The final-run dataset is also more appropriate
311 for use in climate and hydrological studies than the other two datasets are (Tang et al.
312 2016). The IMERG dataset is available online at <https://gpm.nasa.gov/data/directory>.

313 **3.1.4 GSMap Dataset**

314 The GSMap dataset is a satellite-based precipitation dataset constructed by the
315 Core Research for Evolutional Science and Technology program under the authority of
316 the Japan Science and Technology Agency between 2002 and 2007, and the
317 aforementioned program was extended by the JAXA (Ushio et al. 2009; Liu et al.
318 2020a). The GSMap algorithm merges information from various passive microwave
319 sensors of low Earth orbit satellites and infrared sensors on geostationary satellites to
320 create a high-precision precipitation dataset (Kubota et al. 2007). The GSMap dataset
321 is available in near-real-time, post-real-time, and reanalysis versions. The near-real-

322 time versions consists of two datasets: the GSMaP Near Real Time (GSMaP_NRT) and
323 GSMaP Gauge Near Real Time (GSMaP_Gauge_NRT) datasets. The post-real-time
324 versions are the GSMaP Moving Vector with Kalman filter (GSMaP_MVK) and
325 GSMaP_Gauge datasets. Finally, the reanalysis versions are the GSMaP_NRT and
326 GSMaP_Gauge_NRT datasets. This study used the GSMaP_MVK version 7 dataset,
327 which has a temporal resolution of 1 hour, spatial resolution of $0.1^\circ \times 0.1^\circ$, worldwide
328 coverage (60°N to 60°S), and contains data from 2014 to the present. A previous
329 assessment of daily rainfall by using 52 rain gauges in the Philippines from 1998 to
330 2015 revealed that the GSMaP_MVK dataset had a lower level of bias than the TRMM
331 and CMORPH datasets did (Ramos et al. 2016). The hourly GSMaP_MVK version 7
332 dataset can be downloaded from the website of the JAXA
333 (<ftp://rainmap:Niskur+1404@hokusai.eorc.jaxa.jp/standard/v7/hourly/>).

334 **3.1.5 PERSIANN Dataset**

335 The PERSIANN dataset was established by the Center for Hydrometeorology and
336 Remote Sensing at the University of California, Irvine, in association with NASA and
337 the Global Network on Water and Development Information for Arid Lands of the
338 United Nations Educational, Scientific and Cultural Organization. The PERSIANN
339 retrieval algorithm is primarily based on integrated infrared imagery from
340 geosynchronous satellites, with forecasts generated by an artificial neural network to

341 transform infrared imagery into global rainfall data (Sorooshian et al. 2000).
342 PERSIANN includes four precipitation datasets, namely the PERSIANN, the
343 PERSIANN-Cloud Classification System (PERSIANN-CCS), the PERSIANN-
344 Climate Data Record (PERSIANN-CDR), and PERSIANN Dynamic Infrared Rain
345 Rate near-real-time (PDIR-Now) datasets. PERSIANN contains hourly rainfall
346 estimates from March 2000 to the present with a spatial resolution of 0.25° and global
347 coverage (60°N–60°S). PERSIANN-CCS contains hourly rainfall data from January
348 2003 to the present with worldwide coverage and a spatial resolution of 0.04°.
349 PERSIANN-CDR contains daily global rainfall data from January 1983 to the present
350 at a spatial resolution of 0.25°. PDIR-Now contains real-time global precipitation
351 estimates from March 2000 to the present at a spatial resolution of 0.04°. All the
352 PERSIANN datasets are accessible and have been widely used for various studies by
353 researchers and professionals in the fields of climate, hydrology, water resource
354 management, and disaster modeling. This study used the PERSIANN-CCS
355 precipitation dataset, which is available online at <https://chrsdata.eng.uci.edu/>. The
356 spatial resolution of PERSIANN-CCS is higher than that of all the other aforementioned
357 SPDs; thus, the PERSIANN-CCS dataset can be used to examine variations in rainfall
358 in small areas (Rivera et al. 2018).

359 **3.1.6 Wind Data**

360 The wind data used in this study was ERA5, which is a grid reanalysis dataset
361 obtained from the European Centre for Medium-Range Weather Forecasts (ECMWF).
362 ERA5 contains the latest ECMWF atmosphere, land surface, and ocean reanalysis data
363 for global climate monitoring (Hersbach et al. 2020). Through reanalysis, model data
364 containing observations from around the world can be integrated into a complete and
365 worldwide consistent dataset (Olauson, 2018; Ramon et al. 2019; Hersbach et al. 2020).
366 ERA5 is frequently used in various applications and outperforms previous reanalysis
367 methods. It provides long-term (1979 to present) hourly estimates of variables on
368 pressure levels at a spatial resolution of 0.25°. This study used the components u and v
369 of the wind dataset at a pressure level of 925–850 hPa. The aforementioned dataset can
370 be downloaded from [https://cds.climate.copernicus.eu/cdsapp#!/dataset/reanalysis-
371 era5-pressure-levels?tab=form](https://cds.climate.copernicus.eu/cdsapp#!/dataset/reanalysis-era5-pressure-levels?tab=form).

372

373 **3.2 Methods**

374 A point-to-grid comparison was performed to compare the point-based rain gauge
375 measurement data with the grid satellite precipitation dataset and grid reanalysis wind
376 data (Fenta et al. 2018; Liu et al. 2020a). The performance of the SPDs was assessed in
377 terms of the 3-hour temporal scale, rainfall intensity, the terrain, and wind velocity

378 effect by comparing the precipitation estimates with the rain gauge measurements. The
379 comparison between SPDs estimates and rain gauge measurements was carried out
380 when the rain gauge is within R34 during the passing of the storm. The half-hourly
381 IMERG estimation and hourly GSMaP and PERSIANN estimation data were converted
382 into 3-hour rainfall data so that their temporal resolution matched that of the rain gauge
383 measurements. Only a few data points were missing from both the rain gauge stations
384 and SPDs, and they were excluded from the analysis. The 3-hour rainfall estimates
385 obtained by the SPDs were assessed as functions of rainfall intensity. The 3-hour
386 rainfall intensities for all precipitation datasets were categorized into the following five
387 groups: 0–5 mm/3 hours (light rain events), 5–15 mm/3 hours (moderate rain events),
388 15–25 mm/3 hours (heavy rain events), 25–50 mm/3 hours (very heavy rain events),
389 and >50 mm/3 hours (extreme rain events). The performance of the SPDs in terms of
390 the terrain effect was evaluated by dividing the rain gauge stations into two elevation
391 categories: ≤ 1000 m (low altitude) and > 1000 m (high altitude). The evaluation of the
392 SPD performance in terms of wind velocity was conducted by dividing wind speed into
393 the following five categories: 0–5, 5–10, 10–15, 15–20, 20–25, and ≥ 25 m/s. The
394 distribution of the SPD performance in terms of wind direction was modeled as a wind
395 rose, in which wind direction was divided into eight categories: north (N), northeast

396 (NE), east (E), southeast (SE), south (S), southwest (SW), west (W), and northwest
397 (NW).

398 The performance of the SPDs was evaluated by conducting a quantitative analysis
399 of two categories of validation statistics. The first statistical category was continuous
400 statistics, which describe the differences between satellite rainfall magnitude and
401 ground rainfall station measurements and include bias ratio (BR), correlation
402 coefficient (R), mean error (ME), and root mean square error (RMSE). BR refers to the
403 tendency of SPDs to underestimate or overestimate rainfall compared with the rain
404 gauge station measurements. The perfect score for BR is 1. A BR below 1 indicates that
405 the satellite datasets tend to underestimate rainfall compared with the ground rainfall
406 measurements, and a BR above 1 indicates that the satellite datasets tend to
407 overestimate rainfall. The parameter R measures the strength of the linear association
408 between the satellite rainfall estimates and the ground-based observations. A value of
409 1 is the ideal score for R . ME indicates the average error in rainfall measurements
410 between the SPDs and the ground-based observations. RMSE reflects the average
411 deviation in absolute magnitude between the SPD data and the ground-based
412 observations. The ideal value of ME and RSME is 0. RB, R , ME, and RMSE were
413 computed using the following equations (Ebert 2007; Tang et al. 2016; Liu et al. 2020a):

414
$$\text{BR} = \frac{S_i}{G_i} , \quad (1)$$

415
$$R = \frac{\sum_{i=1}^N (S_i - \bar{S})(G_i - \bar{G})}{\sqrt{\sum_{i=1}^N (S_i - \bar{S})^2} \sqrt{\sum_{i=1}^N (G_i - \bar{G})^2}} \quad (2)$$

416
$$ME = \frac{1}{N} \sum_{i=1}^N (S_i - G_i), \quad (3)$$

417
$$RMSE = \sqrt{\frac{1}{N} \sum_{i=1}^N (S_i - G_i)^2}, \quad (4)$$

418 where S_i represents a satellite rainfall estimate, G_i represents the corresponding
 419 ground-based rainfall measurement, \bar{S} indicates the average of the satellite rainfall
 420 estimates, \bar{G} represents the average of the ground-based rainfall measurements, N
 421 represents the total number of data points, and i represents the number of the sample.

422 The second statistical category was volumetric indices, which represent the ability
 423 of SPDs to detect an accurately/inaccurately amount of rainfall. This category includes
 424 volumetric hit index (VHI), volumetric false alarm ratio (VFAR), and volumetric
 425 critical success index (VCSI). VHI provides information regarding the volume of
 426 rainfall accurately detected by the SPDs relative to the volume of rainfall accurately
 427 detected by the satellites and the missing observations. VFAR represents the volume of
 428 false rainfall detected by the SPDs relative to the sum of rainfall detected by the SPDs.
 429 VCSI represents the overall measure of volumetric performance. VHI, VFAR, and
 430 VCSI range from 0 to 1, with the ideal score for VHI and VCSI being 1 and the ideal
 431 score for VFAR being 0. The equations for the volumetric indices are as follows
 432 (Aghakouchak and Mehran 2013; Ayehu et al. 2018; Liu et al. 2020a):

433
$$\text{VHI} = \frac{\sum_{i=1}^N (S_i | (S_i > t \& G_i > t))}{\sum_{i=1}^N (S_i | (S_i > t \& G_i > t)) + \sum_{i=1}^N (G_i | (S_i \leq t \& G_i > t))}, \quad (5)$$

434
$$\text{VFAR} = \frac{\sum_{i=1}^N (S_i | (S_i > t \& G_i \leq t))}{\sum_{i=1}^N (S_i | (S_i > t \& G_i > t)) + \sum_{i=1}^N (S_i | (S_i > t \& G_i \leq t))}, \quad (6)$$

435
$$\text{VCSI} = \frac{\sum_{i=1}^N (S_i | (S_i > t \& G_i > t))}{\sum_{i=1}^N (S_i | (S_i > t \& G_i > t)) + \sum_{i=1}^N (G_i | (S_i \leq t \& G_i > t)) + \sum_{i=1}^N (S_i | (S_i > t \& G_i \leq t))}, \quad (7)$$

436 where t represents the threshold value of 15 mm/3 hours.

437

438 **4 Results and Discussion**

439 The ability of the SPDs to estimate rainfall during heavy precipitation events
 440 caused by typhoons was evaluated in terms of rain rate intensity, elevation, and wind
 441 velocity by using continuous statistics (i.e., BR, R , ME, and RMSE) and volumetric
 442 indices (i.e., VHI, VFAR, and VCSI). High R , VHI, and VCSI values; low ME, RMSE,
 443 and VFAR values; and BR values close to 1 indicated a high performance level.

444 **4.1 Performance of SPDs During Typhoon Events**

445 The agreement between the rain gauge observations and the satellite rainfall
 446 datasets for each typhoon event was determined by using the scatter plots in Figure 2.
 447 In general, in all typhoon events, the satellite rainfall dataset exhibited strong agreement
 448 with the rain gauge observations at low rainfall rates, and this agreement decreased with
 449 increasing rainfall rates. According to the R values, the IMERG dataset exhibited

450 stronger agreement with the rain gauge observations (0.64–0.83) than did the GSMaP
451 (0.39–0.63) and PERSIANN (0.38–0.73) datasets for almost all the typhoons (Sarika,
452 Nock-ten, Doksuri, and Mangkhut). However, the PERSIANN dataset exhibited a
453 stronger agreement with the rain gauge observations ($R = 0.73$) than did the other
454 satellite rainfall datasets during Typhoon Haima. Huang et al. (2019) revealed that the
455 R value for IMERG Final Run version 5 dataset was approximately 0.4–0.63 for six
456 typhoon events in southern China. The current study confirmed that the latest version
457 of the IMERG dataset exhibits increased agreement with the rain gauge observations
458 for higher R values.

459 Table 2 presents a summary of the overall quantitative evaluation of the SPDs and
460 rain gauge measurements during the five typhoon events. The statistic metric summary
461 indicates that three satellite rainfall datasets exhibited different behaviors. This result
462 might have been caused by the complex typhoon structures, different tracks of the
463 typhoons, the structure of the atmosphere, the diverse topographic conditions, and
464 heterogeneous rainfall conditions on the spatiotemporal scale (Huang et al. 2019). The
465 GSMaP dataset substantially overestimated rainfall for all typhoon events compared
466 with the rain gauge data, yielding positive ME (1.75–7.68 mm/3 hours) and BR values
467 (1.22–1.73). ME and BR values greater than 1 were obtained for the aforementioned
468 dataset. A previous study found that GSMaP overestimated the daily extreme

469 precipitation over the Western Himalayas (Parida et al. 2017). Both the IMERG and
470 PERSIANN datasets underestimated rainfall compared with the rain gauge data,
471 yielding negative ME and BR values for all typhoon events. The underestimation of the
472 IMERG dataset in this study is in agreement with the findings of other studies that have
473 applied this dataset to evaluate rainfall in southern China during typhoons Mawar,
474 Pakhar, Hato, and Merbok on a cumulative scale (Huang et al. 2019). In this study, the
475 IMERG dataset outperformed the GSMaP and PERSIANN datasets in terms of ME,
476 BR, and RMSE for all typhoon events except the Doksuri typhoon, for which the ME
477 and BR of the IMERG dataset were marginally higher than those of the PERSIANN
478 dataset.

479 In terms of the ability of the SPDs to detect heavy precipitation events, the GSMaP
480 dataset achieved the highest scores for VHI but the lowest scores for VFAR. The
481 IMERG dataset achieved the highest scores for VFAR (Sarika, Haima, Doksuri, and
482 Mangkhut) and VCSI (Sarika, Haima, Nock-ten, Doksuri, and Mangkhut). The
483 PERSIANN dataset achieved the highest scores for VFAR during the Nock-ten typhoon.
484 To demonstrate the performance of three SPDs more comprehensively, Figure 3
485 presents a performance diagram that displays an overview of the statistics that indicate
486 how well the three SPDs detected heavy precipitation events caused by typhoons in
487 terms of VHI, VFAR, VCSI, and BR. Such a performance diagram was proposed by

488 Roebber to create a visual framework of the association among multiple aspects of
489 model performance (Roebber 2009). VHI is represented on the y -axis; success ratio (1
490 $-$ VFAR) is represented on the x -axis; BR is represented by the dotted lines beginning
491 at the origin, where the diagonal dotted line represents no bias; and VCSI is represented
492 by the dashed contour lines. The best performance is in the top right corner of the
493 diagram and along the diagonal dotted line, where BR is 1. The IMERG dataset
494 achieved the best performance among the SPDs during typhoons Sarika, Haima, Nock-
495 ten, Doksuri, and Mangkhut. This result can probably be attributed to the high temporal
496 resolution of the IMERG dataset when determining the frequency of precipitation
497 events, which allows this dataset to detect the regional variance in subdaily precipitation
498 more effectively (Dezfuli et al. 2017; Liu et al. 2020a).

499 The temporal variation in rainfall is a critical factor in the assessment of extreme
500 weather phenomena and the hydrological cycle (Liu et al. 2016a; Liu et al. 2016b;
501 Huang et al. 2019). Heavy rainfall in a short period can cause natural disasters, such as
502 floods and landslides. Figure 4 presents plots of the average 3-hour rainfall in the
503 Philippines during the five typhoon events. The highest values for average 3-hour
504 rainfall were different for each typhoon event probably due to the differences in
505 atmospheric conditions and the complexity of the typhoon structure. In general, the
506 patterns of temporal variations of precipitation found using the three SPDs were in good

507 agreement with that of rain gauge measurements. The GSMaP dataset exhibited
508 superior agreement with the rainfall station observations during peak rainfall. The
509 IMERG and PERSIANN datasets considerably underestimated rainfall during rainfall
510 peaks in the typhoon events.

511 **4.2 Performance of SPDs Under Different Rainfall Intensities**

512 The BR values between the rain gauge station measurements and the data of the
513 IMERG, GSMaP, and PERSIANN datasets for different rainfall rate intervals were
514 derived. Figure 5 presents a boxplot of the BRs for the IMERG, GSMaP, and
515 PERSIANN datasets during the five typhoon events under different rainfall intensities.
516 The bottom and top of the boxplot represent the first and the third quartiles of the data,
517 respectively. The line inside the boxplot represents the second quartile and median. The
518 maximum and minimum values of the data are represented by the lines at the top and
519 bottom of the whisker, respectively. Outliers are any line not within the whisker. The
520 datasets tended to overestimate rainfall during light to moderate rain (0–5 and 5–15
521 mm/3 hours) and tended to underestimate rainfall during heavy to extreme rain (15–25,
522 25–50, and >50 mm/3 hours). This result is consistent with those of other studies, one
523 of which confirmed that the IMERG and GSMaP datasets overestimate the frequency
524 of light to moderate rainfall events (1–10 mm) and underestimate the frequency of
525 extreme rainfall events (> 0 mm) (Liu et al. 2020a). Another study revealed that the

526 GSMaP and PERSIANN datasets underestimate the frequency of extreme rainfall (75–
527 100 mm/day) (Palharini et al. 2020). Fang et al. (2019) discovered that the IMERG
528 dataset underestimates extreme precipitation. The underestimation of the SPDs during
529 heavy to extreme rainfall might be caused by the interpolation process of classifying
530 heavy rainfall (Fang et al. 2019). The IMERG dataset exhibited a satisfactory ability to
531 detect moderate rainfall events (5–15 mm/3 hours), whereas the GSMaP dataset
532 exhibited superior performance to the other two datasets in detecting heavy to extreme
533 rainfall (15–25, 25–50, and >50 mm/3 hours) during the five typhoon events in the
534 Philippines.

535 The performance of the SPDs was also assessed at various rainfall thresholds: 5,
536 15, 25, and 50 mm/3 hours. Figure 6 presents the performance diagram for the IMERG,
537 GSMaP, and PERSIANN datasets in terms of the volumetric indices (VHI, $1 - VFAR$,
538 VCSI, and BR) for 3-hour precipitation under various rainfall thresholds. The ability of
539 these three SPDs to detect precipitation decreased with an increase in rainfall. VHI and
540 VCSI decreased and VFAR increased with increasing rainfall intensity. These results
541 indicated that the satellite sensors performed poorly in terms of detecting precipitation
542 in extreme rainfall events (Sun et al. 2016; Huang et al. 2019). The IMERG dataset
543 exhibited a stronger rainfall detection ability than did the other two datasets when the
544 rainfall was 5, 15, and 25 mm/3 hours. However, the GSMaP dataset exhibited the

545 strongest ability to detect rainfall when the rainfall was 50 mm/3 hours. The
546 PERSIANN dataset exhibited the weakest ability to detect rainfall at all rainfall rates.
547 Research demonstrated that the PERSIANN dataset did not perform well in the
548 detection of daily moderate rainfall events (10 mm) and daily heavy rainfall events (25
549 mm) in the Wei River Basin in China (Liu et al. 2019). The poor performance of
550 PERSIANN dataset may due to the fact that the precipitation estimation algorithm of
551 PERSIANN is not calibrated with the rain gauge observations. The IMERG dataset is
552 calibrated using the monthly rainfall dataset from the Deutscher Wetterdienst Global
553 Precipitation Climatology Centre (Nguyen et al. 2018; Huffman et al. 2019).

554 **4.3 Performance of the SPDs at Different Elevations**

555 The variation in rainfall in the island area is caused by orographic uplift and the
556 complexity of topography (Lee et al. 2014). Topography has a prominent effect on
557 precipitation (Chen et al. 2020). The altitudes of the rain gauge stations used in this
558 study were divided into two categories: ≤ 1000 m (low altitude) and > 1000 m (high
559 altitude). Table 3 presents an assessment of statistical metrics for the IMERG, GSMaP,
560 and PERSIANN datasets for 3-hour precipitation estimates at different elevations.
561 According to the BR and ME values, the SPDs tended to overestimate rainfall at low
562 elevation and underestimate rainfall at high elevations. The IMERG dataset had the
563 highest R and lowest RMSE values at both high and low altitudes. The IMERG dataset

564 exhibited superior performance at low altitudes because it had the best scores in the
565 continuous statistical analysis (BR, *R*, ME, and RMSE). The BR of the GSMaP dataset
566 was 0.96 at high altitudes, which indicates that this dataset had 4% bias compared with
567 the rain gauge measurements. The high BR of the GSMaP dataset at high elevations
568 was possibly caused by the inclusion of a topographic dataset from the Shuttle Radar
569 Topography Mission 30 Arc Second to classify orographic and nonorographic rainfall
570 (Yamamoto and Shige 2015).

571 Satellite rainfall estimates performed better in detecting heavy precipitation at high
572 altitudes than at low altitudes. This result might have been caused by orographic uplift
573 (Tang et al. 2018). In terms of the ability of SPDs to detect heavy rainfall at different
574 elevations, the PERSIANN dataset exhibited the lowest VHI and VCSI values at low
575 altitudes, whereas the GSMaP dataset exhibited the worse VFAR values at low
576 elevations (Table 3). The GSMaP dataset exhibited the highest VHI at both altitudes;
577 the IMERG dataset exhibited the best VFAR values at low altitudes; and the
578 PERSIANN dataset had a perfect VFAR value at high altitudes. The performance
579 diagram summarizes the three SPDs' ability to detect heavy rainfall accurately at
580 different altitudes (Figure 7). The GSMaP dataset outperformed the other datasets in
581 terms of the ability to detect heavy rainfall at high elevations, whereas the IMERG
582 dataset outperformed the other datasets at low elevations. The PERSIANN dataset

583 performed poorly at both elevations probably because its rainfall estimation algorithm
584 does not contain a terrain component (Nguyen et al. 2018).

585 **4.4 Performance of the SPDs Under Different Wind Velocities**

586 The levels of infrastructural and environmental damage caused by typhoon events
587 are influenced by wind intensity. High wind intensity is also associated with heavy
588 rainfall, which is another hazard of typhoon events (Bloemendaal et al. 2020). In a
589 previous study, the rainfall caused by typhoon events was forecasted using satellite
590 estimates of rainfall data, typhoon intensity, and wind vectors (Kidder et al. 2005). The
591 effect of wind velocity on the ability of SPDs to detect heavy precipitation caused by
592 typhoon events should be investigated. In this study, the averages of the wind vector
593 components u and v from the ECMWF at a pressure level of 925–850 hPa, which is
594 observed at the considered rain gauge stations, were processed into wind speed and
595 direction, respectively. The frequency distribution indicates the relationship between
596 wind speed and the continuous performance statistics (Figure 8). The IMERG and
597 PERSIANN datasets underestimated rainfall compared with the gauge station
598 measurements, yielding a high-frequency concentration of negative MEs (–20–0 mm/3
599 hours) and a BR below 1 for the distribution of wind speed. The GSMaP dataset tended
600 to overestimate rainfall, with a distribution of frequency concentrated on positive MEs
601 (0–20 mm/3 hours) and a BR above 1. The IMERG dataset exhibited superior

602 agreement with the rain gauge observations at different wind speeds, with the
603 distribution frequency of R ranging from 0.4 to 1. For the PERSIANN and GSMaP
604 datasets, the distribution frequency of R ranged from 0.1 to 1 and from 0 to 0.9,
605 respectively. The frequency distributions of RMSE at each wind speed for the IMERG
606 and PERSIANN datasets ranged from 0 to 30 mm/3 hours, whereas those for the
607 GSMaP dataset ranged from 0 to 40 mm/3 hours. Among the three SPDs, the IMERG
608 dataset was the most consistent with the rain gauge measurements in terms of having
609 the most continuous statistical parameters at the different wind speeds. The distribution
610 frequencies of ME, RMSE, R , and BR for the IMERG dataset were concentrated around
611 the near-perfect value for the continuous statistics.

612 The distribution percentage of each volumetric index presented in Figure 9 was
613 used to describe the association between wind speed and the ability of the SPDs to
614 detect heavy rainfall events caused by typhoons. In terms of the VHI distribution, the
615 GSMaP dataset exhibited the best performance, followed by the IMERG and
616 PERSIANN dataset. The GSMaP dataset yielded high frequency distribution for a VHI
617 range of 0.9–1.0 in the wind speed range of 7.5–12.5 m/s. The IMERG dataset exhibited
618 high frequency distribution for a VHI range of 0.9–1.0 in the wind speed range of 10–
619 12.5 m/s, and the PERSIANN dataset exhibited high frequency distribution for a VHI
620 range of 0.5–0.6 in the wind speed range of 7.5–10 m/s. In terms of false rainfall

621 estimates, the IMERG dataset outperformed the GSMaP and PERSIANN datasets. The
622 IMERG dataset had a high-frequency distribution at a lower VFAR than did the other
623 SPDs. The comprehensive evaluation of the volumetric index performance indicates
624 that compared with the other SPDs, the IMERG dataset exhibited a stronger ability to
625 detect heavy rainfall at various wind speeds.

626 Complex topography and mountainous regions with orographic convection and
627 low-troposphere winds represent a challenge in rainfall estimation by satellites (Shige
628 et al. 2013). Luzon, which is located in the northern part of the Philippines, has a
629 complex and mountainous topography and often experiences typhoons. Therefore, the
630 influence of wind in mountainous areas on the performance of satellite rainfall
631 estimations must be studied. Wind direction and speed data were collected from a
632 selected rainfall measurement station on Luzon island (Figure 1b) and analyzed in the
633 form of wind roses. A wind rose is a graph that represents the distribution of wind speed
634 and direction for an area over a certain period. Figure 10a presents a wind rose for the
635 eastern part of the mountainous region, and Figure 10k presents a wind rose for the
636 western part of the region. A total of 75% of the winds are in the NW direction in the
637 eastern part of the mountainous region, and the most frequent wind speed interval is
638 10–15 m/s, which accounts for 50% of the wind speeds. In the eastern part of the
639 mountainous region, wind speed is primarily in the intervals of 10–15, 0–5, 5–10, and

640 15–20 m/s. A total of 41% of the winds in the western part of the mountainous region
641 are in the north direction, and the predominant wind speed is >25 m/s, which accounts
642 for 23% of the wind speeds. In the western part of the mountainous region, wind speed
643 is predominantly in the intervals of >25, 20–25, and 15–20 m/s. This finding indicates
644 that wind speeds are higher in the western part of the mountainous region than in its
645 eastern part.

646 Figure 10(b–j) depicts the distribution of volumetric statistical values for the
647 different wind direction and wind speed ranges in the eastern part of the mountainous
648 region of Luzon. Figure 10(l–t) illustrates the distribution of volumetric statistical
649 values for the western part of the mountainous region. The IMERG dataset
650 outperformed the other SPDs in detecting heavy rainfall events in the eastern part of
651 the mountainous region, as indicated by the distributions of VHI, VFAR, and VCSI.
652 Compared with the other SPDs, the IMERG dataset exhibited superior distributions of
653 VHI, VFAR, and VCSI under almost all ranges of wind speed and wind direction. The
654 GSMaP dataset yielded high VHI and VCSI values for most wind speed ranges and
655 wind directions in the western part of the mountainous region. This result indicated that
656 the GSMaP dataset exhibited a strong performance in detecting heavy rainfall events
657 under high wind speeds. However, the VFAR values of the GSMaP dataset were higher
658 than those of the other SPDs, which were approximately 0.5–1 for the western part of

659 the mountainous area. This result indicates that the GSMaP algorithm generates a large
660 quantity of false rainfall data under high wind speeds. Among the three SPDs, the
661 GSMaP and IMERG datasets demonstrated a stronger ability to detect heavy rainfall
662 events in terms of the effect of wind velocity in the western and eastern parts of the
663 mountainous region, respectively.

664 **5. Conclusion**

665 Assessing the performance of SPDs during heavy precipitation caused by
666 typhoons is crucial for utilizing them and evaluating their algorithms. Studies have
667 analyzed the ability of SPDs to detect heavy precipitation caused by typhoon events on
668 daily, monthly, seasonal, annual, and cumulative scales. This study performed a
669 subdaily (3-hour) assessment of the performance of three SPDs, namely the IMERG,
670 GSMaP, and PERSIANN datasets, during five typhoon-related heavy precipitation
671 events in the Philippines between 2016 and 2018. This assessment was performed
672 through a point-to-pixel comparison by using continuous and volumetric statistical
673 validation indices to assess the R34 values of the typhoons, rainfall intensity, the terrain,
674 and wind velocity effects. This study yielded the following results:

- 675 1. The IMERG dataset exhibited good agreement with the rain gauge
676 observations and performed considerably well in detecting rainfall during the

677 five typhoon events over the Philippines. The GSMaP dataset exhibited
678 superior agreement with the rainfall station observations during peak rainfall.

679 2. The precipitation datasets tended to overestimate rainfall in light to moderate
680 rainfall events and underestimate rainfall in heavy to extreme rainfall events.

681 The IMERG dataset exhibited a strong ability to detect rainfall in moderate
682 rainfall events (5–15 mm/3 hours), whereas the GSMaP dataset exhibited
683 superior performance in detecting rainfall during heavy to extreme rain events
684 (15–25, 25–50, and >50 mm/3 hours) during the five typhoon events in the
685 Philippines.

686 3. The GSMaP dataset outperformed the other SPDs in terms of ability to detect
687 heavy rainfall at high elevations, whereas the IMERG dataset outperformed
688 the other SPDs in terms of ability to detect rainfall at low elevations.

689 4. Wind direction and wind speed influence the ability of SPDs to detect rainfall.
690 The IMERG dataset exhibited a strong ability to detect heavy rainfall under
691 various wind speeds. The GSMaP dataset exhibited a stronger ability to detect
692 heavy rainfall events in terms of wind velocity in the western part of the
693 mountainous region than in its eastern part. By contrast, the IMERG dataset
694 exhibited better performance in the eastern part of the mountainous region than
695 in its western part.

696 The accurate detection and estimation of heavy precipitation with SPDs remains a
697 challenge in archipelagos with complex terrain or mountainous areas. In this study, the
698 IMERG and GSMaP datasets demonstrated a promising ability to detect heavy
699 precipitation caused by typhoon events. An in-depth investigation is required before the
700 IMERG and GSMaP datasets are applied to tropical-cyclone-related studies.
701 Developments in SPD algorithms are expected to focus on improving the detection of
702 extreme rainfall and the use of hourly rain gauge observations for calibration. In the
703 most recent study, the cloud microphysical and optical properties, such as cloud-top
704 altitude, cloud optical thickness and effective cloud droplet radius could be retrieved
705 accurately from the observation of geostationary satellite (e.g, Liu et al., 2020b), and
706 all the cloud properties are associated with the precipitation as already known before.
707 Additional studies might be including the analysis of cloud properties and other typhoon
708 event samples to investigate the precipitation processes and quantify the source of error
709 in SPDs.

710

711 **Declarations**

- 712 ● **Availability of data and materials:** Please contact author for data requests.
- 713 ● **Funding:** This work was supported by the Ministry of Science and Technology of
714 Taiwan (grants MOST 109-2625-M-008-013, MOST 109-2111-M-008-025,

715 MOST 110-2625-M-008-002, and MOST 110-2111-M-008-033) and Academia
716 Sinica (grants AS-TP-107-M10-3 and AS-GC-110-01).

717 ● **Competing interests:** The authors declare that they have no competing interests.

718 ● **Author's Contributions:** CYL conceived and designed this study. PA performed
719 the data analysis and wrote the original draft. All the authors discussed the results
720 and reviewed, edited, and commented on the manuscript. All the authors read and
721 approved the final version of this manuscript for publication.

722 ● **Acknowledgments:** We credit the providers of the IMERG, GSMaP, and
723 PERSIANN datasets. We also acknowledge PAGASA, Department of Science and
724 Technology, Republic of the Philippines, for its support in obtaining gauge station
725 rainfall data across the Philippines. PA was supported by the International Ph.D.
726 Program in Environmental Science and Technology (University System of Taiwan)
727 at National Central University, Taiwan. This work was supported by the Ministry
728 of Science and Technology of Taiwan (grants MOST 109-2625-M-008-013,
729 MOST 109-2111-M-008-025, MOST 110-2625-M-008-002, and MOST 110-
730 2111-M-008-033) and Academia Sinica (grants AS-TP-107-M10-3 and AS-GC-
731 110-01).

732

733 **References**

- 734 Aghakouchak A, Mehran A (2013) Extended contingency table: Performance metrics
735 for satellite observations and climate model simulations. *Water Resources*
736 *Research* 49:7144–7149. <https://doi.org/10.1002/wrcr.20498>
- 737 Ayehu GT, Tadesse T, Gessesse B, Dinku T (2018) Validation of new satellite rainfall
738 products over the Upper Blue Nile Basin, Ethiopia. *Atmospheric Measurement*
739 *Techniques* 11:1921–1936. <https://doi.org/10.5194/amt-11-1921-2018>
- 740 Bagtasa G (2017) Contribution of tropical cyclones to rainfall in the Philippines.
741 *Journal of Climate* 30:3621–3633. <https://doi.org/10.1175/JCLI-D-16-0150.1>
- 742 Bautista L (2011) Philippine territorial boundaries: internal tensions, colonial baggage,
743 ambivalent conformity. *JATI : Journal of Southeast Asian Studies* 16:35–53
- 744 Beck HE, Van Dijk AIJM, Levizzani V, et al (2017) MSWEP: 3-hourly 0.25° global
745 gridded precipitation (1979–2015) by merging gauge, satellite, and reanalysis data.
746 *Hydrology and Earth System Sciences* 21:589–615. [https://doi.org/10.5194/hess-](https://doi.org/10.5194/hess-21-589-2017)
747 [21-589-2017](https://doi.org/10.5194/hess-21-589-2017)
- 748 Bell JL, Sloan LC, Snyder MA (2004) Regional changes in extreme climatic events: A
749 future climate scenario. *Journal of Climate* 17:81–87.
750 [https://doi.org/10.1175/1520-0442\(2004\)017<0081:RCIECE>2.0.CO;2](https://doi.org/10.1175/1520-0442(2004)017<0081:RCIECE>2.0.CO;2)
- 751 Bloemendaal N, de Moel H, Muis S, et al (2020) Estimation of global tropical cyclone
752 wind speed probabilities using the STORM dataset. *Scientific Data* 7:1–11.
753 <https://doi.org/10.1038/s41597-020-00720-x>
- 754 Chen C, Li Z, Song Y, et al (2020) Performance of multiple satellite precipitation
755 estimates over a typical arid mountainous area of China: Spatiotemporal patterns
756 and extremes. *Journal of Hydrometeorology* 21:533–550.
757 <https://doi.org/10.1175/JHM-D-19-0167.1>
- 758 Chen S, Hong Y, Cao Q, et al (2013) Performance evaluation of radar and satellite
759 rainfalls for Typhoon Morakot over Taiwan: Are remote-sensing products ready
760 for gauge denial scenario of extreme events? *Journal of Hydrology* 506:4–13.
761 <https://doi.org/10.1016/j.jhydrol.2012.12.026>
- 762 Chen TC, Wu CC (2016) The remote effect of Typhoon Megi (2010) on the heavy
763 rainfall over Northeastern Taiwan. *Monthly Weather Review* 144:3109–3131.
764 <https://doi.org/10.1175/MWR-D-15-0269.1>
- 765 Cheung K, Yu Z, Elsberry RL, et al (2018) Recent Advances in Research and
766 Forecasting of Tropical Cyclone Rainfall. *Tropical Cyclone Research and Review*

767 7:106–127. <https://doi.org/10.6057/2018TCRR02.03>

768 Cinco TA, de Guzman RG, Ortiz AMD, et al (2016) Observed trends and impacts of
769 tropical cyclones in the Philippines. *International Journal of Climatology*
770 36:4638–4650. <https://doi.org/10.1002/joc.4659>

771 Dezfuli AK, Ichoku CM, Huffman GJ, et al (2017) Validation of IMERG Precipitation
772 in Africa. *Journal of Hydrometeorology* 18:2817–2825.
773 <https://doi.org/10.1175/JHM-D-17-0139.1>

774 Duan Z, Liu J, Tuo Y, et al (2016) Evaluation of eight high spatial resolution gridded
775 precipitation products in Adige Basin (Italy) at multiple temporal and spatial scales.
776 *Science of the Total Environment* 573:1536–1553.
777 <https://doi.org/10.1016/j.scitotenv.2016.08.213>

778 Ebert EE (2007) Methods for Verifying Satellite Precipitation Estimates. In: *Measuring*
779 *Precipitation from Space: EURAINSAT and the Future*. Springer, pp 345–356

780 Fang J, Yang W, Luan Y, et al (2019) Evaluation of the TRMM 3B42 and GPM IMERG
781 products for extreme precipitation analysis over China. *Atmospheric Research*
782 223:24–38. <https://doi.org/10.1016/j.atmosres.2019.03.001>

783 Fenta AA, Yasuda H, Shimizu K, et al (2018) Evaluation of satellite rainfall estimates
784 over the Lake Tana basin at the source region of the Blue Nile River. *Atmospheric*
785 *Research* 212:43–53. <https://doi.org/10.1016/j.atmosres.2018.05.009>

786 Funk C, Peterson P, Landsfeld M, et al (2015) The climate hazards infrared precipitation
787 with stations - A new environmental record for monitoring extremes. *Scientific*
788 *Data* 2:1–21. <https://doi.org/10.1038/sdata.2015.66>

789 Hersbach H, Bell B, Berrisford P, et al (2020) The ERA5 global reanalysis. *Quarterly*
790 *Journal of the Royal Meteorological Society* 146:1999–2049.
791 <https://doi.org/10.1002/qj.3803>

792 Hon K-K (2020) Tropical cyclone track prediction using a large-area WRF model at the
793 Hong Kong Observatory. *Tropical Cyclone Research and Review* 9:67–74.
794 <https://doi.org/10.1016/j.tcr.2020.03.002>

795 Hong Y, Alder R, Huffman G (2006) Evaluation of the potential of NASA multi-satellite
796 precipitation analysis in global landslide hazard assessment. *Geophysical*
797 *Research Letters* 33:1–5. <https://doi.org/10.1029/2006GL028010>

798 Hou AY, Kakar RK, Neeck S, et al (2014) The global precipitation measurement
799 mission. *Bulletin of the American Meteorological Society* 95:701–722.
800 <https://doi.org/10.1175/BAMS-D-13-00164.1>

801 Hsu K, Gao X, Sorooshian S, Gupta H V. (1997) Precipitation Estimation from
802 Remotely Sensed Information Using Artificial Neural Networks. *Journal of*
803 *Applied Meteorology* 36:1176–1190. [https://doi.org/10.1175/1520-](https://doi.org/10.1175/1520-0450(1997)036<1176:pefrsi>2.0.co;2)
804 [0450\(1997\)036<1176:pefrsi>2.0.co;2](https://doi.org/10.1175/1520-0450(1997)036<1176:pefrsi>2.0.co;2)

805 Huang C, Hu J, Chen S, et al (2019) How Well Can IMERG Products Capture Typhoon
806 Extreme Precipitation Events over Southern China? *Remote Sensing* 11:70.
807 <https://doi.org/10.3390/rs11010070>

808 Huang X, Wang D, Liu Y, et al (2018) Evaluation of extreme precipitation based on
809 satellite retrievals over China. *Frontiers of Earth Science* 12:846–861.
810 <https://doi.org/10.1007/s11707-017-0643-2>

811 Huang YC, Lin YL (2014) A study on the structure and precipitation of Morakot (2009)
812 induced by the Central Mountain Range of Taiwan. *Meteorology and Atmospheric*
813 *Physics* 123:115–141. <https://doi.org/10.1007/s00703-013-0290-4>

814 Huffman GJ, Bolvin DT, Braithwaite D, et al (2019) Algorithm Theoretical Basis
815 Document (ATBD) Version 06 NASA Global Precipitation Measurement (GPM)
816 Integrated Multi-satellitE Retrievals for GPM (IMERG). National Aeronautics and
817 Space Administration (NASA) 1–34

818 Jamandre CA, Narisma GT (2013) Spatio-temporal validation of satellite-based rainfall
819 estimates in the Philippines. *Atmospheric Research* 122:599–608.
820 <https://doi.org/10.1016/j.atmosres.2012.06.024>

821 Javanmard S, Yatagai A, Nodzu MI, et al (2010) Comparing high-resolution gridded
822 precipitation data with satellite rainfall estimates of TRMM-3B42 over Iran.
823 *Advances in Geosciences* 25:119–125. [https://doi.org/10.5194/adgeo-25-119-](https://doi.org/10.5194/adgeo-25-119-2010)
824 [2010](https://doi.org/10.5194/adgeo-25-119-2010)

825 Ji X, Li Y, Luo X, et al (2020) Evaluation of bias correction methods for APHRODITE
826 data to improve hydrologic simulation in a large Himalayan basin. *Atmospheric*
827 *Research* 242:104964. <https://doi.org/10.1016/j.atmosres.2020.104964>

828 Jones SC, Harr PA, Abraham J, et al (2003) The extratropical transition of tropical
829 cyclones: Forecast challenges, current understanding, and future directions.
830 *Weather and Forecasting* 18:1052–1092. [https://doi.org/10.1175/1520-](https://doi.org/10.1175/1520-0434(2003)018<1052:TETOTC>2.0.CO;2)
831 [0434\(2003\)018<1052:TETOTC>2.0.CO;2](https://doi.org/10.1175/1520-0434(2003)018<1052:TETOTC>2.0.CO;2)

832 Joyce RJ, Janowiak JE, Arkin PA, Xie P (2004) CMORPH: A Method that Produces
833 Global Precipitation Estimates from Passive Microwave Microwave and Infrared
834 Data at High Spatial and Temporal Resolution. *Journal of Hydrometeorology*
835 5:487–502. <https://doi.org/10.1175/1525->

836 7541(2004)005<0487:CAMTPG>2.0.CO;2

837 Kidder SQ, Kusselson SJ, Knaff JA, et al (2005) The tropical rainfall potential (TRaP)
838 technique. Part I: Description and examples. *Weather and Forecasting* 20:456–464.
839 <https://doi.org/10.1175/WAF860.1>

840 Kimball SK (2008) Structure and evolution of rainfall in numerically simulated
841 landfalling hurricanes. *Monthly Weather Review* 136:3822–3847.
842 <https://doi.org/10.1175/2008MWR2304.1>

843 Knapp KR, Kruk MC, Levinson DH, et al (2010) The international best track archive
844 for climate stewardship (IBTrACS). *Bulletin of the American Meteorological*
845 *Society* 91:363–376. <https://doi.org/10.1175/2009BAMS2755.1>

846 Kubota H, Wang B (2009) How much do tropical cyclones affect seasonal and
847 interannual rainfall variability over the western North Pacific? *Journal of Climate*
848 22:5495–5510. <https://doi.org/10.1175/2009JCLI2646.1>

849 Kubota T, Hashizume H, Shige S, et al (2007) Global precipitation map using
850 satelliteborne microwave radiometers by the GSMaP project: Production and
851 validation. *IEEE Transactions on Geoscience and Remote Sensing* 45:2584–2587.
852 <https://doi.org/10.1109/IGARSS.2006.668>

853 Lee K-O, Uyeda H, Lee D-I (2014) Microphysical structures associated with
854 enhancement of convective cells over Mt. Halla, Jeju Island, Korea on 6 July 2007.
855 *Atmospheric Research* 135–136:76–90.
856 <https://doi.org/10.1016/j.atmosres.2013.08.012>

857 Levizzani V, Cattani E (2019) Satellite remote sensing of precipitation and the terrestrial
858 water cycle in a changing climate. *Remote Sensing* 11:.
859 <https://doi.org/10.3390/rs11192301>

860 Li Z, Yang D, Hong Y (2013) Multi-scale evaluation of high-resolution multi-sensor
861 blended global precipitation products over the Yangtze River. *Journal of*
862 *Hydrology* 500:157–169. <https://doi.org/10.1016/j.jhydrol.2013.07.023>

863 Liu C.-Y., Aryastana P, Liu G-R, Huang W-R (2020a) Assessment of satellite
864 precipitation product estimates over Bali Island. *Atmospheric Research* 244:1–14.
865 <https://doi.org/10.1016/j.atmosres.2020.105032>

866 Liu C.-Y., C.-H.Chiu, P. H.Lin, and M. Min (2020b) Comparison of Cloud-Top Property
867 Retrievals From Advanced Himawari Imager, MODIS, CloudSat/CPR,
868 CALIPSO/CALIOP, and Radiosonde. *J. Geophys. Res. Atmos.*, 125,
869 <https://doi.org/10.1029/2020JD032683>.

870 Liu C.-Y., Kuo S-C, Lim A, et al (2016a) Optimal Use of Space-Borne Advanced

871 Infrared and Microwave Soundings for Regional Numerical Weather Prediction.
872 Remote Sensing 8:816. <https://doi.org/10.3390/rs8100816>

873 Liu C.-Y., Li J, Ho S-P, et al (2016b) Retrieval of Atmospheric Thermodynamic State
874 From Synergistic Use of Radio Occultation and Hyperspectral Infrared Radiances
875 Observations. IEEE Journal of Selected Topics in Applied Earth Observations and
876 Remote Sensing 9:744–756. <https://doi.org/10.1109/JSTARS.2015.2444274>

877 Liu J, Xia J, She D, et al (2019) Evaluation of six satellite-based precipitation products
878 and their ability for capturing characteristics of extreme precipitation events over
879 a climate transition area in China. Remote Sensing 11:1–21.
880 <https://doi.org/10.3390/rs11121477>

881 Lonfat M, Rogers R, Marchok T, Marks FD (2007) A parametric model for predicting
882 hurricane rainfall. Monthly Weather Review 135:3086–3097.
883 <https://doi.org/10.1175/MWR3433.1>

884 Nashwan MS, Shahid S, Dewan A, et al (2020) Performance of five high resolution
885 satellite-based precipitation products in arid region of Egypt: An evaluation.
886 Atmospheric Research 236:104809.
887 <https://doi.org/10.1016/j.atmosres.2019.104809>

888 Nguyen P, Ombadi M, Sorooshian S, et al (2018) The PERSIANN family of global
889 satellite precipitation data: A review and evaluation of products. Hydrology and
890 Earth System Sciences 22:5801–5816. <https://doi.org/10.5194/hess-22-5801-2018>

891 Okamoto K, Ushio T, Iguchi T, et al (2005) The Global Satellite Mapping of
892 Precipitation (GSMaP) project. International Geoscience and Remote Sensing
893 Symposium (IGARSS) 5:3414–3416.
894 <https://doi.org/10.1109/IGARSS.2005.1526575>

895 Olauson J (2018) ERA5: The new champion of wind power modelling? Renewable
896 Energy 126:322–331. <https://doi.org/10.1016/j.renene.2018.03.056>

897 PAGASA Climate of the Philippines.
898 <http://bagong.pagasa.dost.gov.ph/information/climate-philippines#>. Accessed 10
899 Oct 2020

900 Palharini RSA, Vila DA, Rodrigues DT, et al (2020) Assessment of the extreme
901 precipitation by satellite estimates over South America. Remote Sensing 12:1–24.
902 <https://doi.org/10.3390/rs12132085>

903 Parida BR, Behera SN, Bakimchandra O, et al (2017) Evaluation of satellite-derived
904 rainfall estimates for an extreme rainfall event over Uttarakhand, Western
905 Himalayas. Hydrology 4:1–18. <https://doi.org/10.3390/hydrology4020022>

- 906 Pham NTT, Vu HH (2020) Characteristics of Tropical Cyclone Precipitating System
907 Along Central Coastal Region of Vietnam by TRMM and GSMAP Data. In: The
908 10th International Conference on Asian and Pacific Coasts (APAC) 2019. Springer
909 Nature Singapore Pte Ltd., Hanoi, pp 87–91
- 910 Pombo S, de Oliveira RP (2015) Evaluation of extreme precipitation estimates from
911 TRMM in Angola. *Journal of Hydrology* 523:663–679.
912 <https://doi.org/10.1016/j.jhydrol.2015.02.014>
- 913 Ramon J, Lledó L, Torralba V, et al (2019) What global reanalysis best represents near-
914 surface winds? *Quarterly Journal of the Royal Meteorological Society* 145:3236–
915 3251. <https://doi.org/10.1002/qj.3616>
- 916 Ramos MD, Tendencia E, Espana K, et al (2016) Assessment of satellite precipitation
917 products in the philippine archipelago. *International Archives of the*
918 *Photogrammetry, Remote Sensing and Spatial Information Sciences - ISPRS*
919 *Archives XLI-B1:423–427*. [https://doi.org/10.5194/isprsarchives-XLI-B1-423-](https://doi.org/10.5194/isprsarchives-XLI-B1-423-2016)
920 2016
- 921 Rashid I, Parray AA, Romshoo SA (2018) Evaluating the Performance of Remotely
922 Sensed Precipitation Estimates against In-Situ Observations during the September
923 2014 Mega-Flood in the Kashmir Valley. *Asia-Pacific Journal of Atmospheric*
924 *Sciences* 55:209–219. <https://doi.org/10.1007/s13143-018-0071-6>
- 925 Rivera JA, Marianetti G, Hinrichs S (2018) Validation of CHIRPS precipitation dataset
926 along the Central Andes of Argentina. *Atmospheric Research* 213:437–449.
927 <https://doi.org/10.1016/j.atmosres.2018.06.023>
- 928 Roebber PJ (2009) Visualizing multiple measures of forecast quality. *Weather and*
929 *Forecasting* 24:601–608. <https://doi.org/10.1175/2008WAF2222159.1>
- 930 Ross RJ, Kurihara Y (1995) A Numerical Study on Influences of Hurricane Gloria (1985)
931 on the Environment. *Monthly Weather Review* 123:332–346.
932 [https://doi.org/10.1175/1520-0493\(1995\)123<0332:ANSOIO>2.0.CO;2](https://doi.org/10.1175/1520-0493(1995)123<0332:ANSOIO>2.0.CO;2)
- 933 Setiawati MD, Miura F, Aryastana P (2016) Validation of Hourly GSMaP and ground
934 base estimates of precipitation for flood monitoring in Kumamoto, Japan. In:
935 Srivastava PK, Pandey PC, Kumar P, et al. (eds) *Geospatial Technology for Water*
936 *Resource Applications*. CRC Press, Boca Raton : Taylor & Francis, 2017., pp 130–
937 143
- 938 Shige S, Kida S, Ashiwake H, et al (2013) Improvement of TMI Rain Retrievals in
939 Mountainous Areas. *Journal of Applied Meteorology and Climatology* 52:242–
940 254. <https://doi.org/10.1175/JAMC-D-12-074.1>

- 941 Sorooshian S, Hsu KL, Gao X, et al (2000) Evaluation of PERSIANN system satellite-
942 based estimates of tropical rainfall. *Bulletin of the American Meteorological*
943 *Society* 81:2035–2046. [https://doi.org/10.1175/1520-0477\(2000\)081<2035:EOPSSE>2.3.CO;2](https://doi.org/10.1175/1520-0477(2000)081<2035:EOPSSE>2.3.CO;2)
944
- 945 Stampoulis D, Anagnostou EN, Nikolopoulos EI (2013) Assessment of high-resolution
946 satellite-based rainfall estimates over the mediterranean during heavy precipitation
947 events. *Journal of Hydrometeorology* 14:1500–1514.
948 <https://doi.org/10.1175/JHM-D-12-0167.1>
- 949 Sun R, Yuan H, Liu X, Jiang X (2016) Evaluation of the latest satellite–gauge
950 precipitation products and their hydrologic applications over the Huaihe River
951 basin. *Journal of Hydrology* 536:302–319.
952 <https://doi.org/10.1016/j.jhydrol.2016.02.054>
- 953 Tang G, Behrangi A, Long D, et al (2018) Accounting for spatiotemporal errors of
954 gauges: A critical step to evaluate gridded precipitation products. *Journal of*
955 *Hydrology* 559:294–306. <https://doi.org/10.1016/j.jhydrol.2018.02.057>
- 956 Tang G, Ma Y, Long D, et al (2016) Evaluation of GPM Day-1 IMERG and TMPA
957 Version-7 legacy products over Mainland China at multiple spatiotemporal scales.
958 *Journal of Hydrology* 533:152–167. <https://doi.org/10.1016/j.jhydrol.2015.12.008>
- 959 Tashima T, Kubota T, Mega T, et al (2020) Precipitation Extremes Monitoring Using
960 the Near-Real-Time GSMaP Product. *IEEE Journal of Selected Topics in Applied*
961 *Earth Observations and Remote Sensing* 13:5640–5651.
962 <https://doi.org/10.1109/jstars.2020.3014881>
- 963 Ushio T, Sasashige K, Kubota T, et al (2009) A Kalman Filter Approach to the Global
964 Satellite Mapping of Precipitation (GSMaP) from Combined Passive Microwave
965 and Infrared Radiometric Data. *Journal of the Meteorological Society of Japan*
966 87A:137–151. <https://doi.org/10.2151/jmsj.87A.137>
- 967 Wang D, Wang X, Liu L, et al (2016) Evaluation of CMPA precipitation estimate in the
968 evolution of typhoon-related storm rainfall in Guangdong, China. *Journal of*
969 *Hydroinformatics* 18:1055–1068. <https://doi.org/10.2166/hydro.2016.241>
- 970 Wang Y, Wang Y, Fudeyasu H (2009) The role of Typhoon Songda (2004) in producing
971 distantly located heavy rainfall in Japan. *Monthly Weather Review* 137:3699–
972 3716. <https://doi.org/10.1175/2009MWR2933.1>
- 973 Weinkle J, Maue R, Pielke R (2012) Historical global tropical cyclone landfalls. *Journal*
974 *of Climate* 25:4729–4735. <https://doi.org/10.1175/JCLI-D-11-00719.1>
- 975 Wu CC, Cheung KKW, Lo YY (2009) Numerical study of the rainfall event due to the

976 interaction of typhoon Babs (1998) and the northeasterly monsoon. *Monthly*
977 *Weather Review* 137:2049–2064. <https://doi.org/10.1175/2009MWR2757.1>

978 Wu H, Adler RF, Hong Y, et al (2012) Evaluation of Global Flood Detection Using
979 Satellite-Based Rainfall and a Hydrologic Model. *Journal of Hydrometeorology*
980 13:1268–1284. <https://doi.org/10.1175/jhm-d-11-087.1>

981 Wu Y, Zhang Z, Huang Y, et al (2019) Evaluation of the GPM IMERG v5 and TRMM
982 3B42 v7 precipitation products in the Yangtze River basin, China. *Water*
983 (Switzerland) 11:. <https://doi.org/10.3390/w11071459>

984 Xie P, Arkin PA (1997) Global Precipitation: A 17-Year Monthly Analysis Based on
985 Gauge Observations, Satellite Estimates, and Numerical Model Outputs. *Bulletin*
986 *of the American Meteorological Society* 78:2539–2558.
987 [https://doi.org/10.1175/1520-0477\(1997\)078<2539:GPAYMA>2.0.CO;2](https://doi.org/10.1175/1520-0477(1997)078<2539:GPAYMA>2.0.CO;2)

988 Yamamoto MK, Shige S (2015) Implementation of an orographic/nonorographic
989 rainfall classification scheme in the GSMaP algorithm for microwave radiometers.
990 *Atmospheric Research* 163:36–47.
991 <https://doi.org/10.1016/j.atmosres.2014.07.024>

992 Yang MJ, Braun SA, Chen DS (2011) Water budget of Typhoon Nari (2001). *Monthly*
993 *Weather Review* 139:3809–3828. <https://doi.org/10.1175/MWR-D-10-05090.1>

994 Yokoyama C, Takayabu YN (2008) A statistical study on rain characteristics of tropical
995 cyclones using TRMM satellite data. *Monthly Weather Review* 136:3848–3862.
996 <https://doi.org/10.1175/2008MWR2408.1>

997 Yu CK, Cheng LW (2013) Distribution and mechanisms of orographic precipitation
998 associated with typhoon morakot (2009). *Journal of the Atmospheric Sciences*
999 70:2894–2915. <https://doi.org/10.1175/JAS-D-12-0340.1>

1000 Yu Z, Yu H, Chen P, et al (2009) Verification of tropical cyclone-related satellite
1001 precipitation estimates in mainland China. *Journal of Applied Meteorology and*
1002 *Climatology* 48:2227–2241. <https://doi.org/10.1175/2009JAMC2143.1>

1003 Zhang F, Weng Y, Kuo YH, et al (2010) Predicting typhoon morakot’s catastrophic
1004 rainfall with a convection-permitting mesoscale ensemble system. *Weather and*
1005 *Forecasting* 25:1816–1825. <https://doi.org/10.1175/2010WAF2222414.1>

1006

1007

1008

1009

1010 **Tables**

1011 Table 1. Information regarding five typhoon events in the Philippines.

Name of Typhoon	Start Time (UTC)	End time (UTC)	Duration (hours)	Maximum Wind Speed (knots)	Number of stations	Maximum Actual Rainfall Rate (mm/3 hours)	Maximum Cumulative Actual Rainfall (mm)
Sarika	2016-10-14 15:00	2016-10-16 12:00	45	95	31	167.0	629.5
Haima	2016-10-18 21:00	2016-10-20 12:00	39	115	15	247.0	836.5
Nock-ten	2016-12-24 12:00	2016-12-26 9:00	45	105	16	183.0	284.0
Doksuri	2017-09-11 6:00	2017-09-12 15:00	33	40	21	151.5	436.0
Mangkhut	2018-09-13 18:00	2018-09-15 21:00	51	148	40	93.5	344.0

1012

1013

1014 Table 2. Statistical metric summary of the Integrated Merged Multisatellite Retrievals
 1015 for Global Precipitation Measurement (IMERG), Global Satellite Mapping of
 1016 Precipitation (GSMaP), and Precipitation Estimation from Remotely Sensed
 1017 Information Using Artificial Neural Networks (PERSIANN) datasets for the five
 1018 typhoon events. Unit of the mean error (ME) and root mean square error (RMSE): mm/3
 1019 hours.

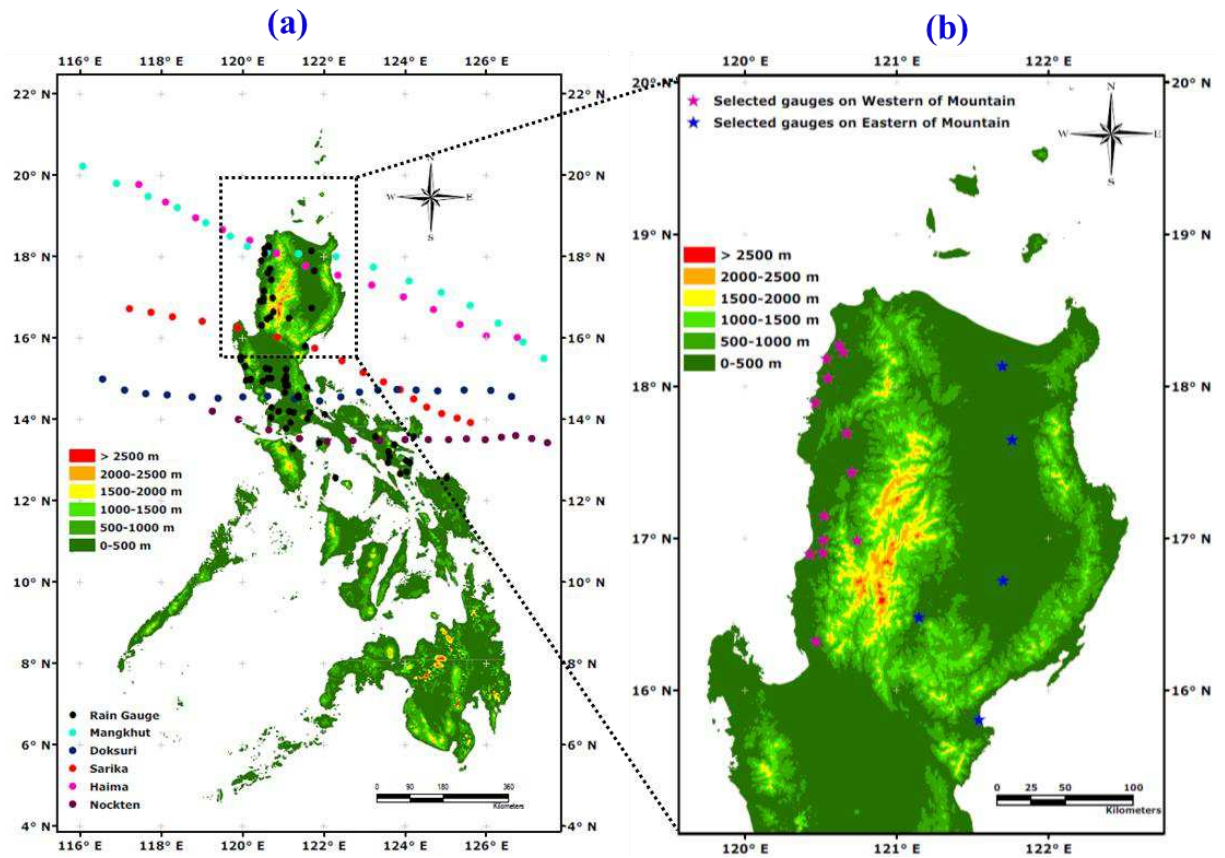
Name of Typhoon	SPD	BR	R	ME	RMSE	VHI	VFAR	VCSI
Sarika	IMERG	0.95	0.72	-2.06	12.51	0.67	0.29	0.52
	GSMaP	1.73	0.62	2.08	16.31	0.77	0.52	0.41
	PERSIANN	0.91	0.55	-2.69	14.89	0.48	0.48	0.33
Haima	IMERG	0.88	0.71	-4.95	21.35	0.59	0.34	0.46
	GSMaP	1.22	0.63	5.49	27.07	0.68	0.44	0.45
	PERSIANN	0.81	0.73	-7.99	22.41	0.51	0.38	0.39
Nock-ten	IMERG	0.97	0.83	-0.93	15.65	0.70	0.28	0.55
	GSMaP	1.35	0.56	2.91	24.23	0.69	0.48	0.42
	PERSIANN	0.73	0.68	-4.02	17.36	0.60	0.18	0.53
Doksuri	IMERG	0.89	0.64	-3.60	14.60	0.55	0.38	0.42
	GSMaP	1.42	0.39	7.68	28.00	0.56	0.60	0.30
	PERSIANN	0.99	0.38	-1.35	19.22	0.45	0.54	0.29
Mangkhut	IMERG	0.97	0.68	-0.40	12.44	0.57	0.41	0.41
	GSMaP	1.29	0.57	1.75	14.37	0.67	0.48	0.41
	PERSIANN	0.84	0.51	-1.11	13.94	0.48	0.43	0.35
All Typhoon	IMERG	0.93	0.72	-2.39	15.31	0.62	0.34	0.47
	GSMaP	1.40	0.55	3.98	22.00	0.67	0.50	0.40
	PERSIANN	0.86	0.57	-3.43	17.56	0.50	0.40	0.38

1020
 1021

1022 Table 3. Statistical metric summary of the IMERG, GSMaP, and PERSIANN datasets
 1023 at different elevations. Unit of ME and RMSE: mm/3 hours.

Elevation	SPD	BR	R	ME	RMSE	VHI	VFAR	VCSI
Low	IMERG	1.08	0.70	1.70	13.25	0.64	0.38	0.45
	GSMaP	1.43	0.55	3.57	19.12	0.66	0.54	0.38
	PERSIANN	1.09	0.52	1.94	15.59	0.52	0.50	0.34
High	IMERG	0.71	0.81	-6.78	17.79	0.54	0.23	0.47
	GSMaP	0.94	0.76	-5.16	18.91	0.74	0.22	0.62
	PERSIANN	0.50	0.74	-9.72	20.51	0.50	0.00	0.50

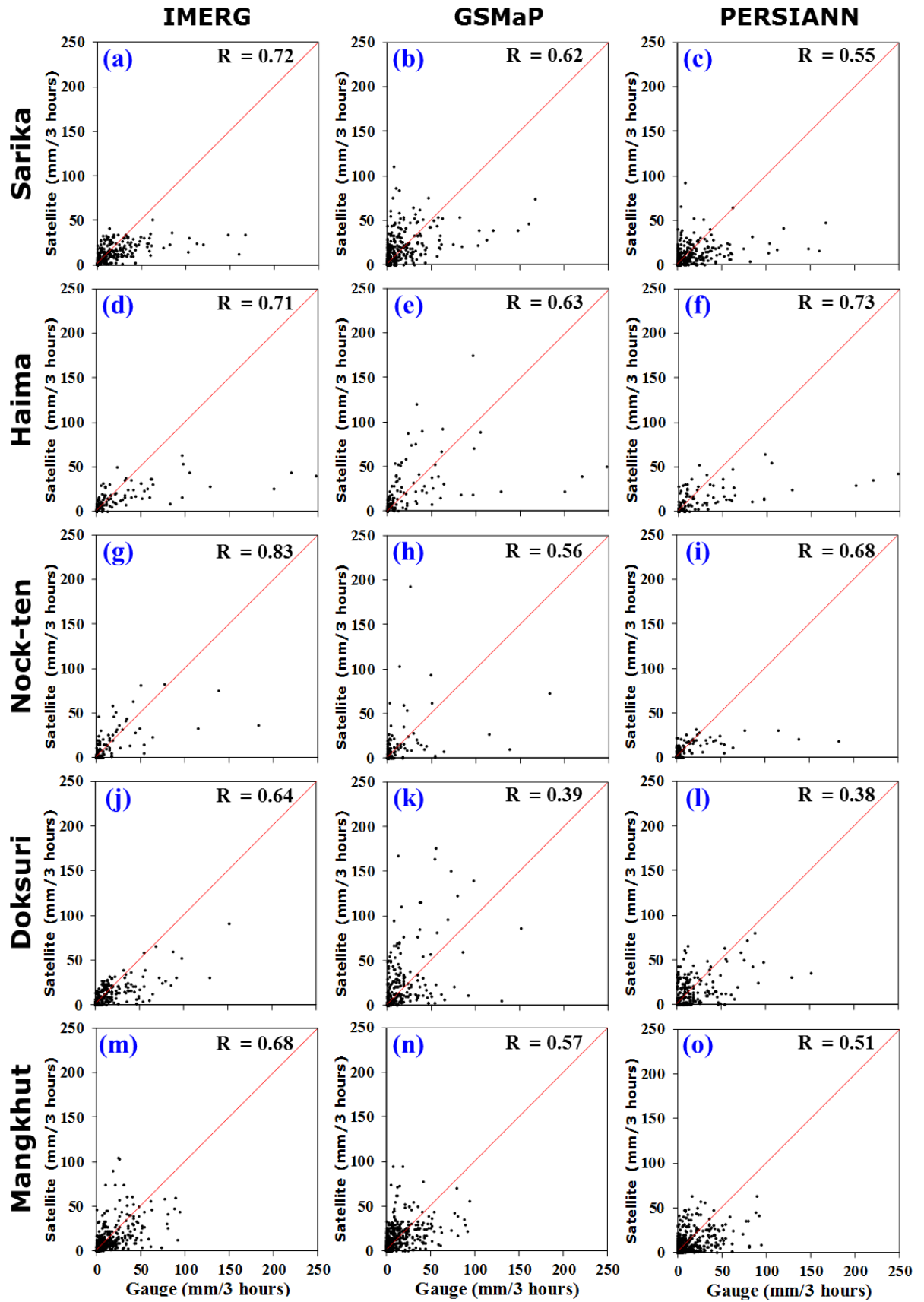
1024
 1025



1026

1027 Figure 1. (a) Map of the Philippines, including distribution of the rain gauge stations
 1028 (black dots), terrain, and tracks of the five typhoons (colored dots). (b) Map of Luzon
 1029 island, including the selected rain gauge stations (colored stars) and terrain.

1030



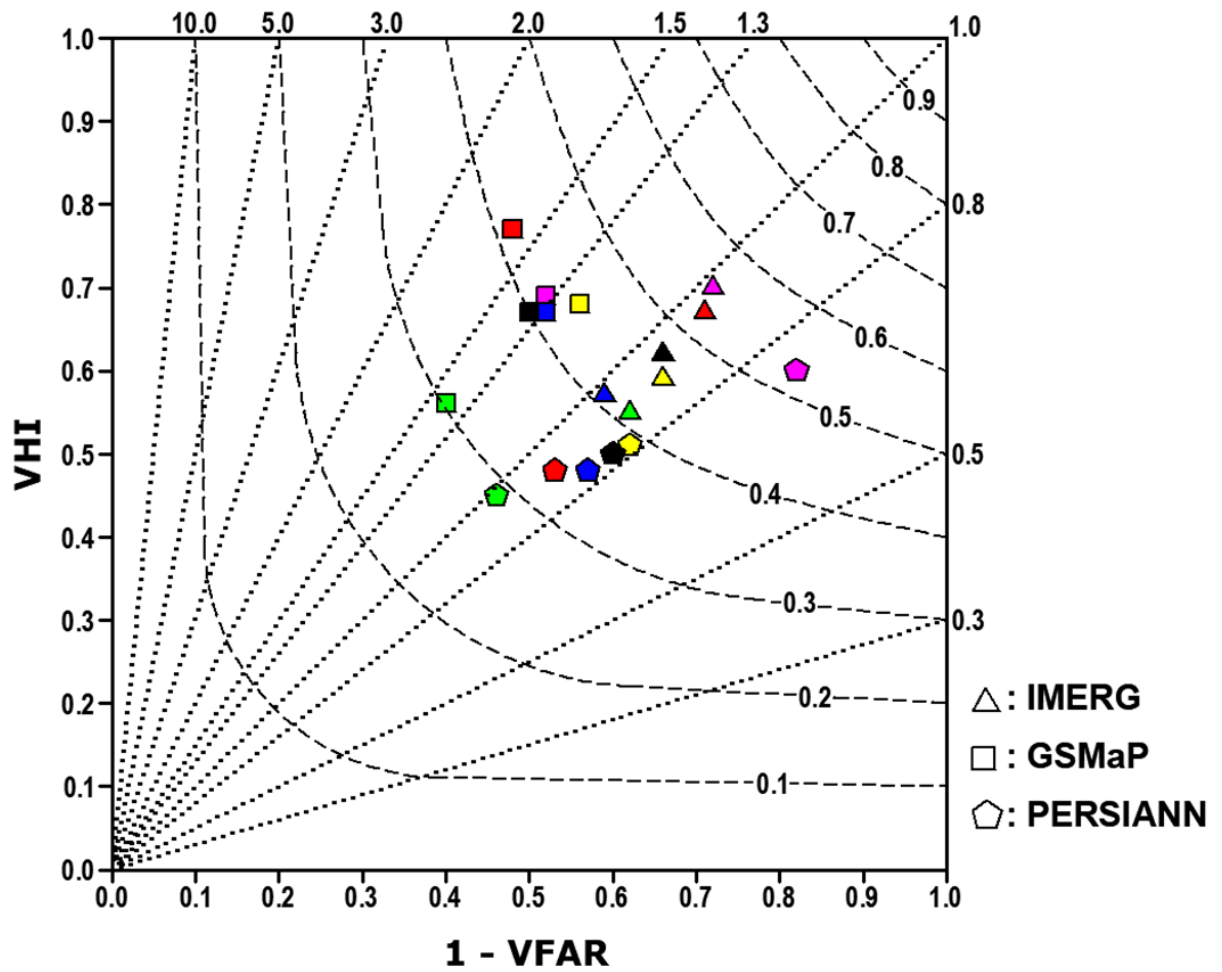
1031

1032

1033

Figure 2. Scatter plot of rain gauge measurements for different satellite precipitation datasets (IMERG, GSMaP, and PERSIANN) during the five typhoon events: Sarika (a–

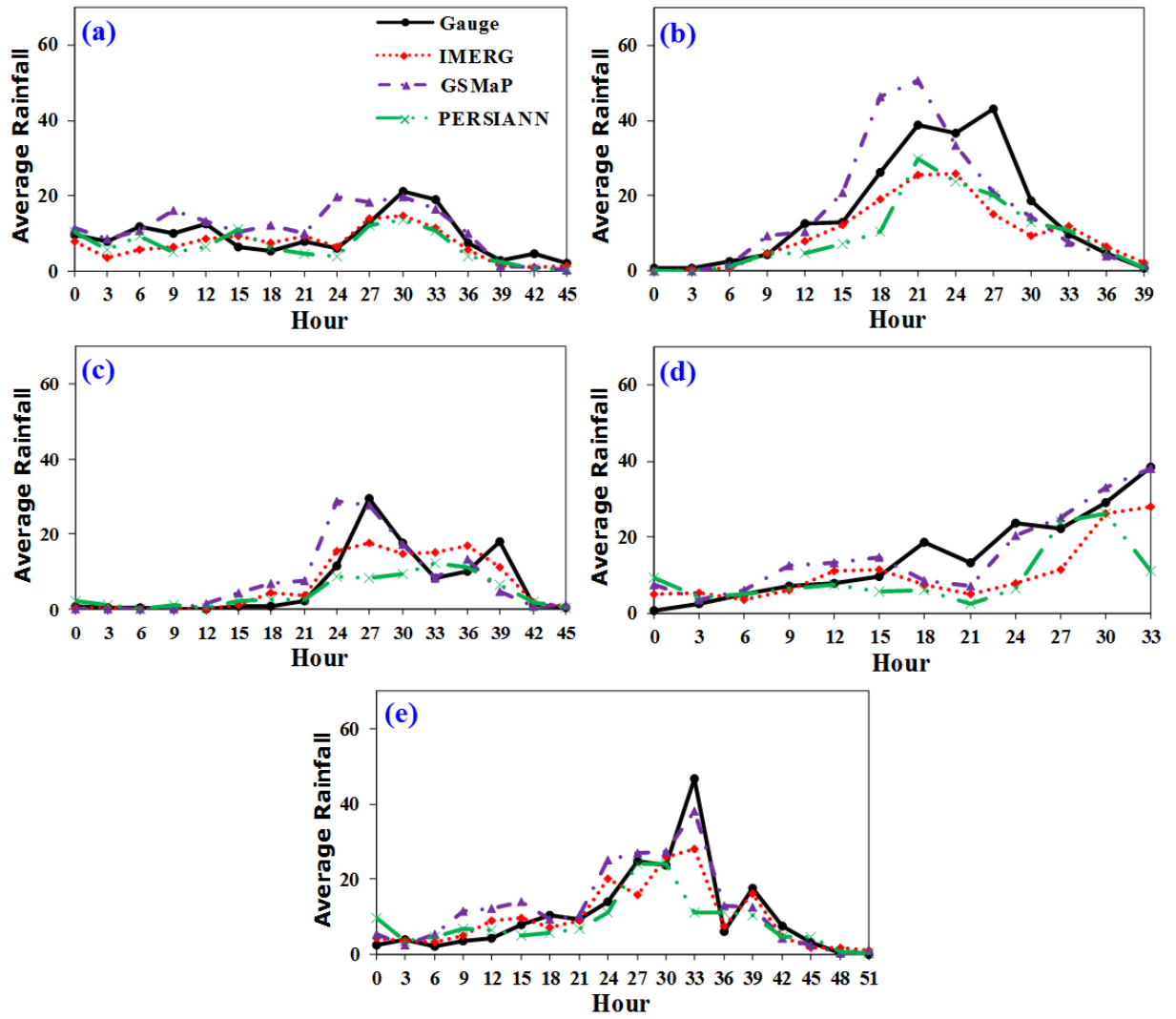
1034 c), Haima (d–f), Nock-ten (g–i), Doksuri (j–l), and Mangkhut (m–o). The parameter R
1035 represents the correlation coefficient.



1036

1037 Figure 3. Performance diagram for the SPDs that represents their ability to detect
 1038 rainfall during typhoon events. Different colors represent different typhoon events (red:
 1039 Sarika; yellow: Haima; magenta: Nock-ten; green: Doksuri; blue: Mangkhut; and black:
 1040 all typhoons).

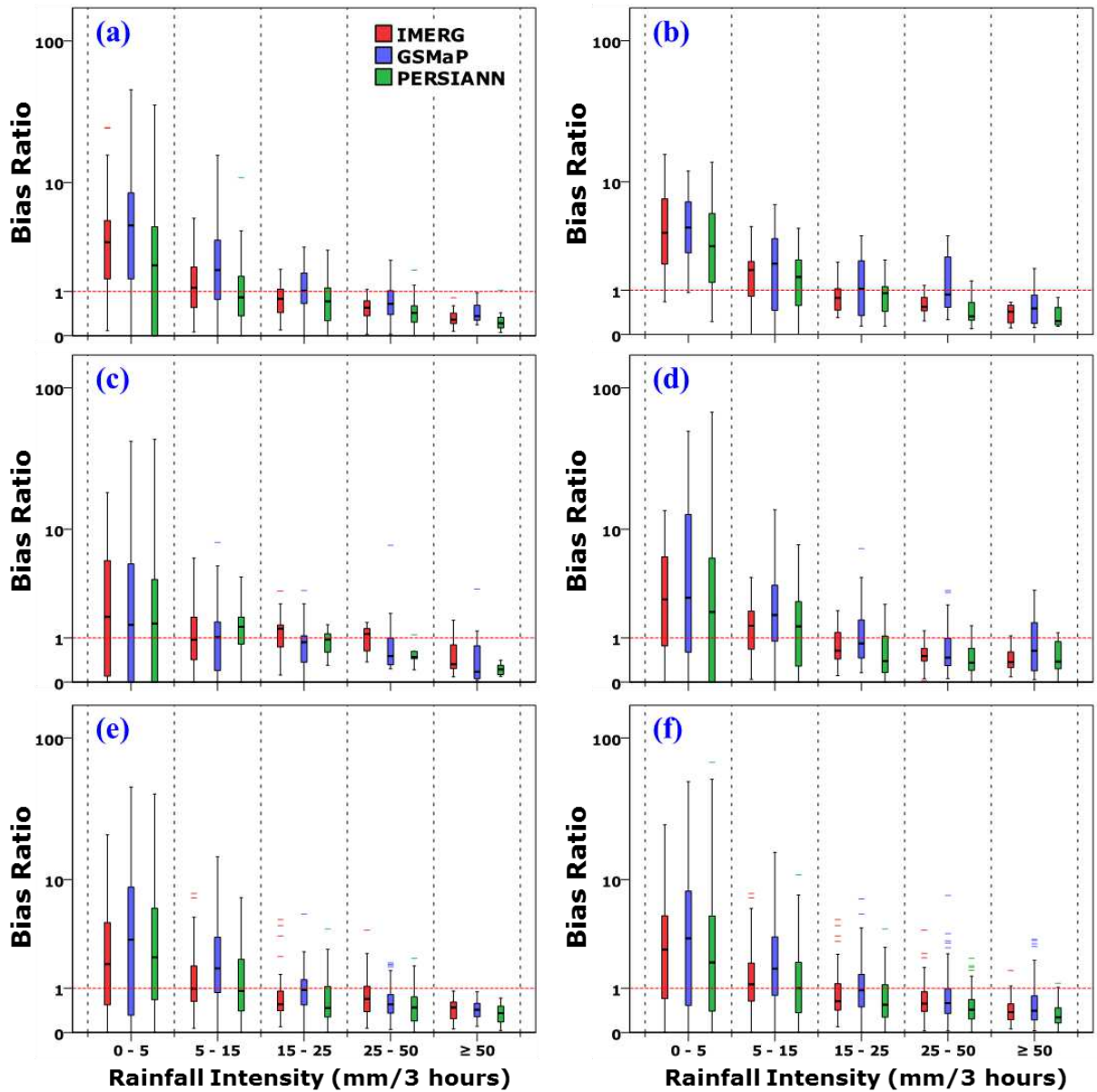
1041



1042

1043 Figure 4. Average 3-hour rainfall during the five typhoon events: (a) Sarika, (b) Haima,
 1044 (c) Nock-ten, (d) Doksuri, and (e) Mangkhut.

1045



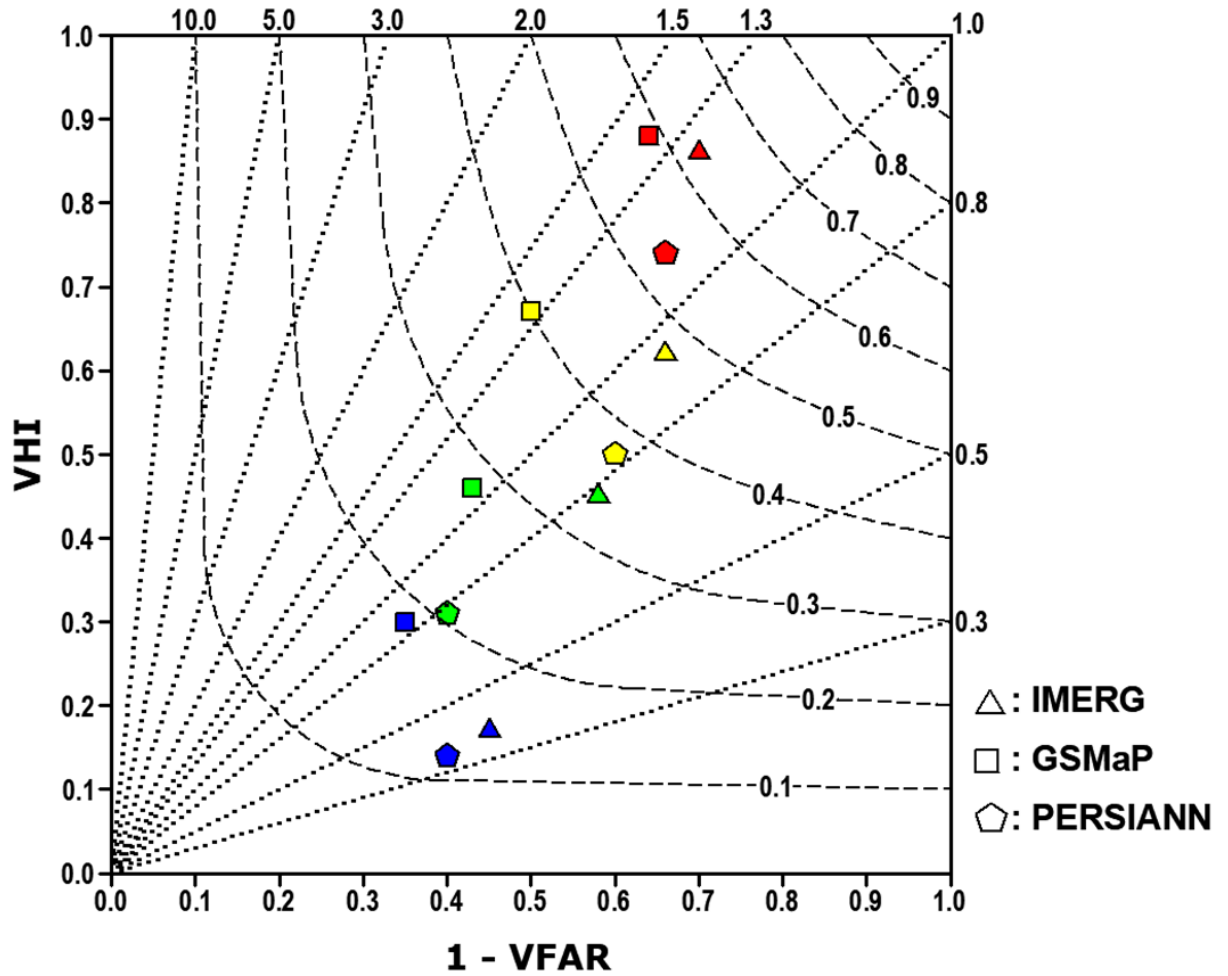
1046

1047 Figure 5. Boxplot of the bias ratios (BRs) for different rainfall intensities for the IMERG,

1048 GSMaP, and PERSIANN datasets during the typhoon events: (a) Sarika, (b) Haima, (c)

1049 Nock-ten, (d) Doksuri, (e) Mangkhut, and (f) all typhoons.

1050



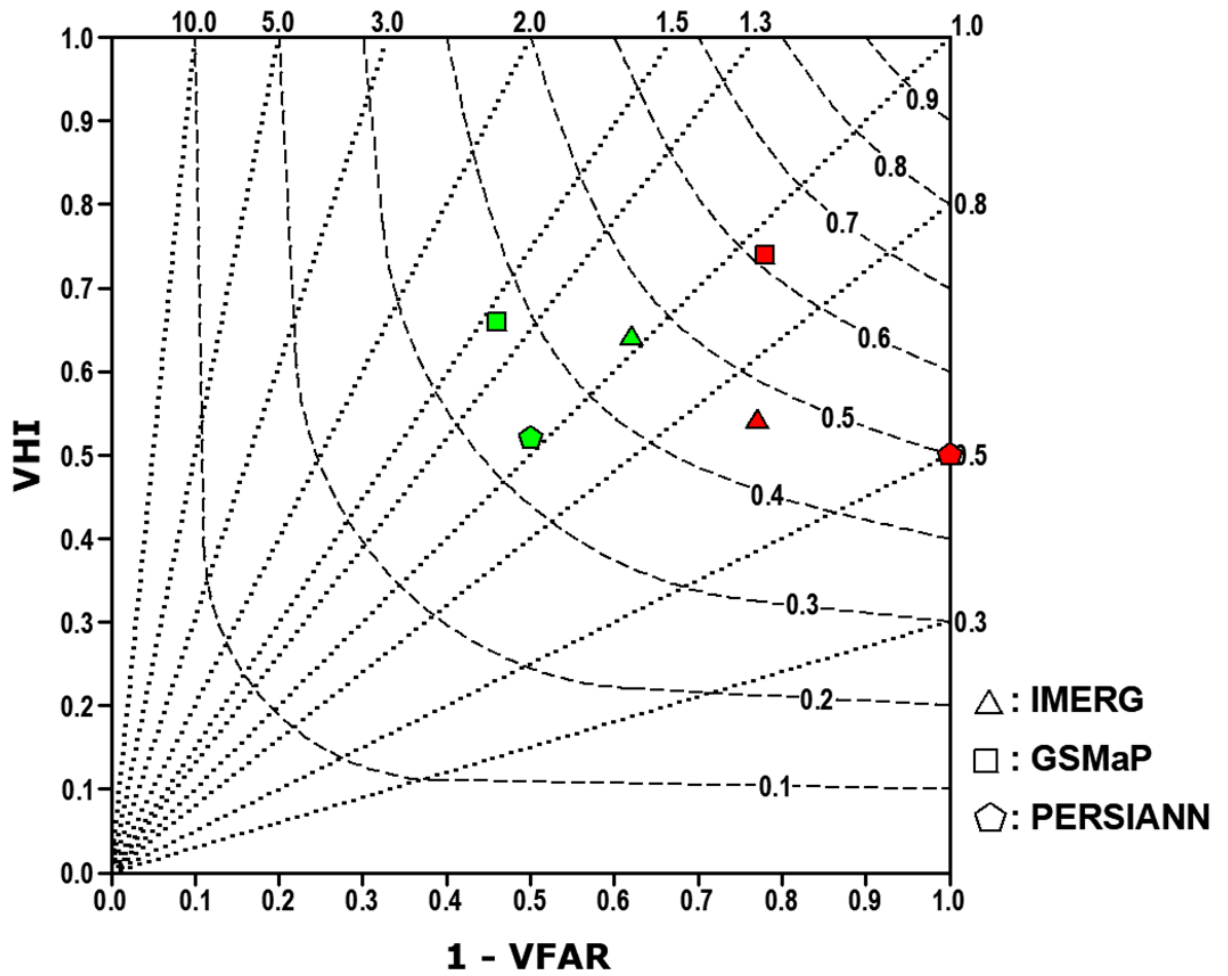
1051

1052 Figure 4. Performance diagram of the SPDs at different threshold values. Different

1053 colors represent different threshold values (red: 5 mm/3 hours; yellow: 15 mm/3 hours;

1054 green: 25 mm/3 hours; and blue: 50 mm/3 hours).

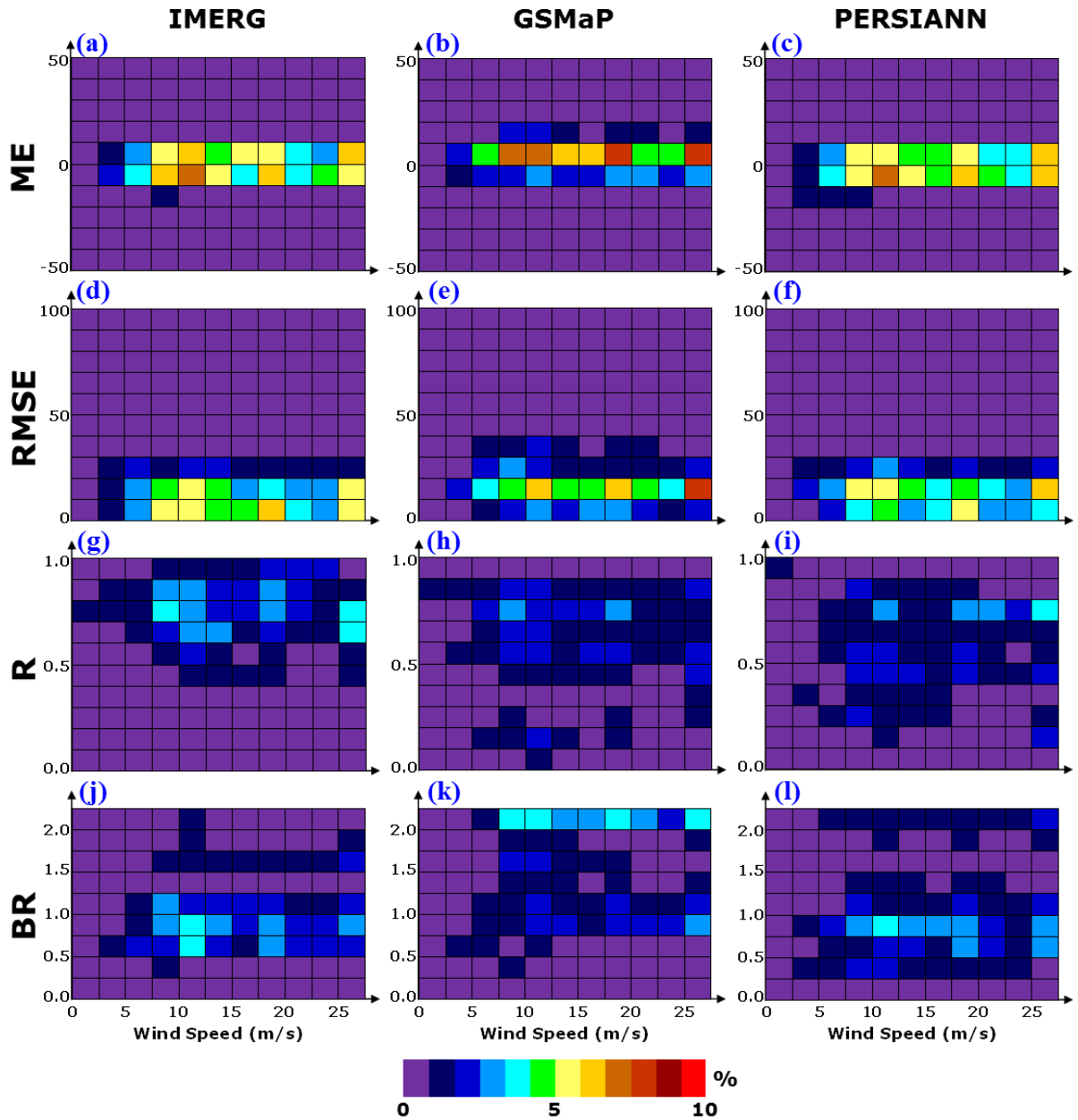
1055



1056

1057 Figure 5. Performance diagram of the SPDs at different altitudes. Different colors
 1058 represent different altitudes (green: low altitude and red: high altitude).

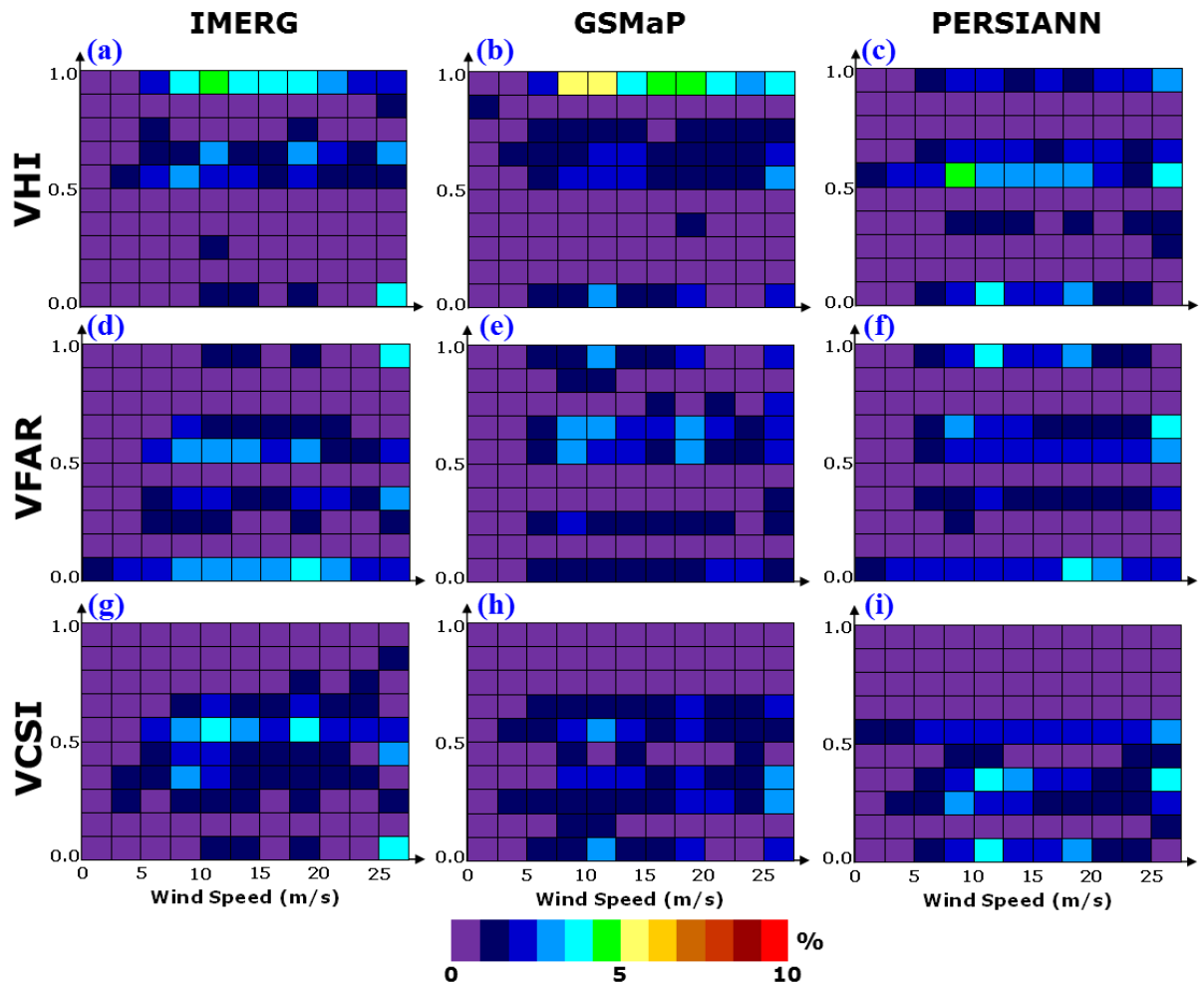
1059



1060

1061 Figure 6. Distribution percentage of each continuous statistic for the IMERG, GSMaP,
 1062 and PERSIANN datasets at different wind speeds: (a–c) ME, (d–f) RMSE, (g–i) R , and
 1063 (j–l) BR. The ME and RMSE value are presented in mm/3 hours.

1064



1065

1066

1067 Figure 9. Distribution percentage of each volumetric index for the IMERG, GSMaP,

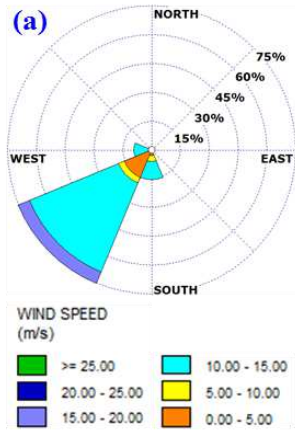
1068 (a–c) volumetric hit index (VHI),

1069 (d–f) volumetric false alarm ratio (VFAR), and (g–i) volumetric critical success index

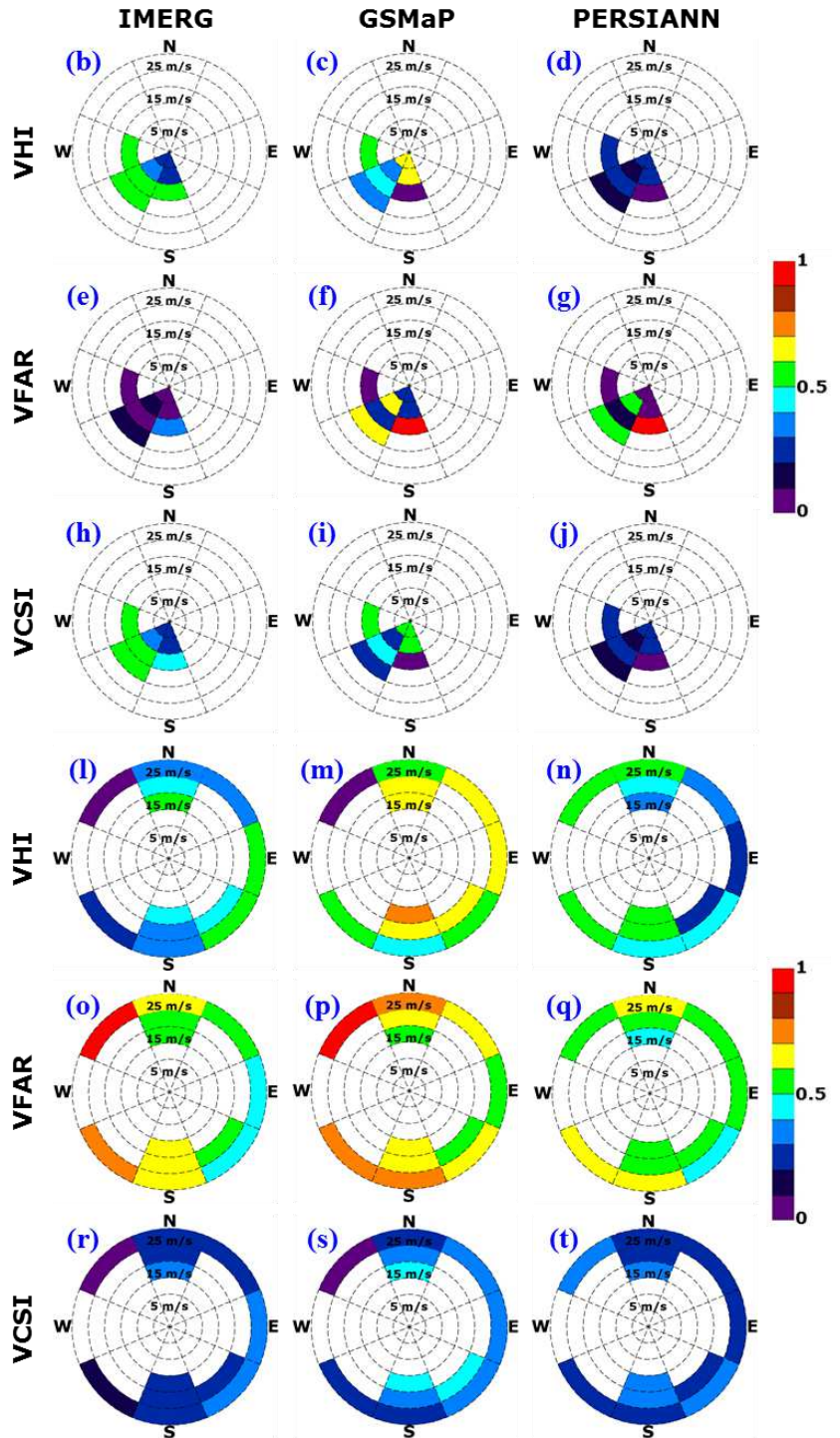
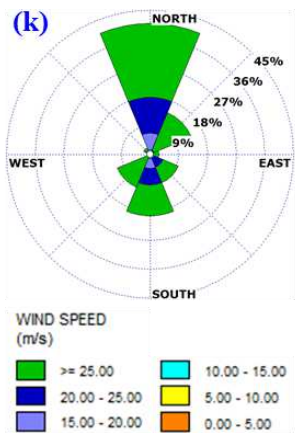
1070 (VCSI).

1070

EASTERN PART OF MOUNTAIN REGION



WESTERN PART OF MOUNTAINOUS REGION



1071

1072 Figure 10. Three-hour, eight-sector wind rose and distribution of volumetric indices for
 1073 the IMERG, GSMaP, and PERSIANN datasets for different wind directions and wind
 1074 speed ranges on Luzon island: (a) wind rose for the eastern part of the mountainous
 1075 region, (b–d) VHI for the eastern part of the mountainous region, (e–g) VFAR for the
 1076 eastern part of the mountainous region, (h–j) VHI for the eastern part of the
 1077 mountainous region, (k) wind rose for the western part of the mountainous region, (l–
 1078 n) VHI for the western part of the mountainous region, (o–q) VFAR for the western part

1079 of the mountainous region, and (r-t) VHI for the western part of the mountainous region.
1080
1081